Geological Magazine

www.cambridge.org/geo

Original Article

**Cite this article:** Zhang N, Liu Z, Xu Z, Li G, Dong X, Liu J, and Li W (2023) Tectonic evolution of the Middle-Late Permian orogenic belt in the eastern part of the CAOB: Implications from the magmatism in the Changchun-Kaiyuan area. *Geological Magazine* **160**: 1875–1892. https://doi.org/10.1017/S001675682300078X

Received: 21 May 2023
Revised: 15 November 2023
Accepted: 27 November 2023
First published online: 10 January 2024

**Keywords:**
Northern margin of the North China Craton; middle-Late Permian; Paleo-Asian Ocean; slab break-off

**Corresponding author:**
Zhenghong Liu; Email: zhliu@jlu.edu.cn



# Tectonic evolution of the Middle-Late Permian orogenic belt in the eastern part of the CAOB: Implications from the magmatism in the Changchun-Kaiyuan area

Nuo Zhang[1,2], Zhenghong Liu[1,2], Zhongyuan Xu[1,2], Gang Li[1,2], Xiaojie Dong[1,2], Jin Liu[1,2] and Wenqing Li[1,2]

[1]College of Earth Sciences, Jilin University, Changchun, China and [2]Key Laboratory of Mineral Resources Evaluation in Northeast Asia, Ministry of Natural Resources, Changchun, China

## Abstract

Various magmatisms during the subduction-collision process are crucial to reveal the long-term tectonic evolution of the eastern Central Asian Orogenic Belt. In this paper, we present major and trace elements of whole-rock, zircon U-Pb dating and Hf isotope of the Shanmen pluton. Results imply that the Shanmen pluton consists of quartz diorite and mylonitic granite, with zircon U-Pb ages of 263.7–259.6 Ma. The studied quartz diorite contains high Sr/Y (51.19–90.87) and $(La/Yb)_N$ (7.82–13.62) ratios, and belongs to adakitic rocks. Coupled with the positive $\varepsilon_{Hf}(t)$ values of +5.71 to +12.8 with no obvious Eu anomaly, we propose that quartz diorite is the product of the interaction between different degrees of slab melt and the overlying mantle wedge. In contrast, the mylonitic granite has lower MgO (0.28 wt% – 0.47 wt%) contents and positive $\varepsilon_{Hf}(t)$ values of +7.79 to +10.15, indicating an affinity with I-type granite originated by partial melting of the intermediate-basic lower crust. The geochemical characteristics and lithological assemblages, along with the Permian magmatic rocks in the Changchun-Kaiyuan area displaying arc rocks affinity, propose their formation is related to the southward subduction of the Paleo-Asian Ocean (PAO). Based on this study and previous evidence, we lean towards adopting a middle-late Permian slab break-off model, wherein the PAO did not close until the late Permian.

## 1. Introduction

The subduction zone plays a crucial role in the interaction of convergent plates resulting in various magmas and serving as a typical accretion orogenic system. A comprehensive understanding of the evolution of subduction zones, including its initiation and termination, as well as associated magmatic, metamorphic and tectonic processes, is essential for revealing crustal growth and circulation, palaeogeographic reconstruction and long-term evolution of the Earth's structure (Crameri *et al.* 2020; Soret *et al.* 2022). The Central Asian Orogenic Belt (CAOB) lies between the Siberian Craton to the north and the Tarim and North China Cratons (NCC) to the south (Şengör *et al.* 1993; Fig. 1a). It is the longest and most complex typical Phanerozoic accretionary orogenic belt on Earth, and it is composed of a wide range of tectonic units, including micro-continents, magma arc, ophiolites, relics of fore-arc and back-arc basins and subduction-accretion complexes (Şengör *et al.* 1993; Wilde *et al.* 2000; Xiao *et al.* 2003, 2015; Zhang *et al.* 2022). Typically, Solonker-Xar Moron-Changchun-Yanji Suture (SXCYS) was regarded to be a sign of the closure of the PAO (Wu *et al.* 2000, 2007a, 2011; Xiao *et al.* 2003, 2015; Liu *et al.* 2021; Fig. 1b).

In Paleozoic, the North-east (NE) China, which is part of the eastern CAOB, underwent closure of the Paleo-Asian Ocean (PAO) and amalgamation of the NCC with several microcontinental massifs, from west to east, including the Erguna, Xing'an, Songliao-Xilinhot and Jiamusi blocks (Liu *et al.* 2017, 2019; Windley *et al.* 2007; Fig. 1b). Some researchers argued that it also consists of a curved Erguna-Jiamusi continent ribbon, early Paleozoic Xing'an-Zhangguancailing accretionary terranes and late Paleozoic Songliao accretionary terranes with some Precambrian micro-block relics in the core area of the orocline (Liu *et al.* 2021, 2022, 2023). However, the tectonic evolution history in the eastern CAOB is still debated, and there is no consensus on the closure time of the PAO and its branches, which range from the Devonian (Xu *et al.* 2013; Zhao *et al.* 2016) to the Late Permian-Early Triassic (Jia *et al.* 2004; Jian *et al.* 2010; Cao *et al.* 2013; Xue, 2021). Furthermore, more tectonic models have been proposed to explain the tectonic affiliation of the eastern PAO during the Permian. These models include the continental rift model (Shao *et al.* 2015), continent-continent collision model (Zhang *et al.*

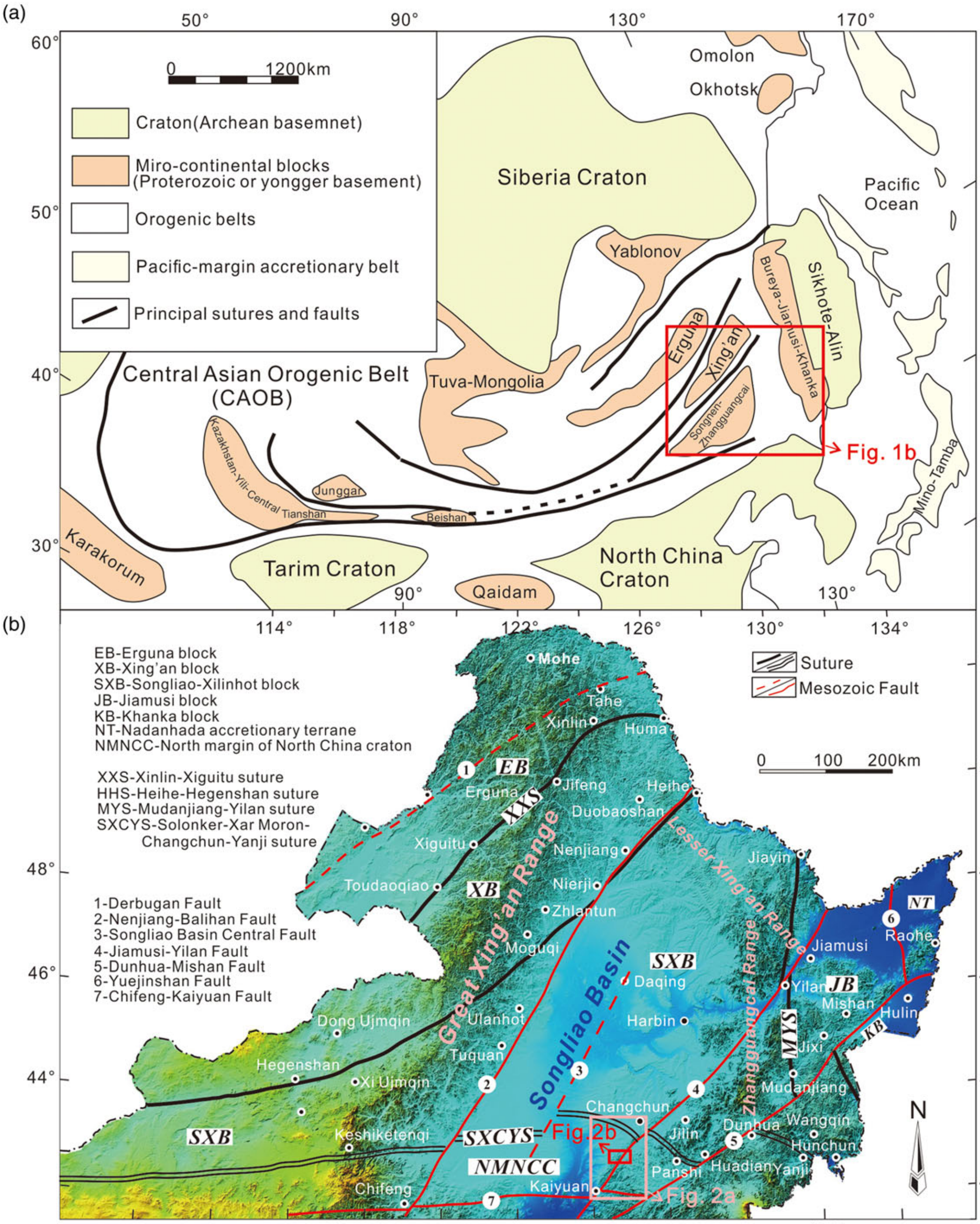


**Figure 1.** (Colour online) (a) Simplified tectonic sketch map of the eastern Central Asian Orogenic Belt (modified after Sengör *et al.* 1993; Zhang *et al.* 2022); (b) Simplified tectonic sketch map of Northeast China (modified after Liu *et al.* 2017).

2007), post-orogenic extension model (Zhang *et al.* 2007; Zhao *et al.* 2008), slab break-off model (Yuan *et al.* 2016) and slab roll-back model (Li *et al.* 2016, 2017).

In this paper, we present zircon U-Pb dating, major and trace elements of whole-rock and zircon Hf isotope of the Shanmen pluton, combined with various data of Permian chronological and geochemical data in the Changchun-Kaiyuan area, to analyse the activity times, rock combination, tectonic environment and the relationship with the PAO.

## 2. Geological background

The Shanmen area in Jilin Province is located at the intersection of Daheishan Horst and SXCYS, bounded by the Shanmen Fault (Siping-Changchun-Dehui Fault) and Yilan-Yitong Fault, which belongs to the eastern part of the northern margin of the NCC (Fig. 2a). Owing to the alteration and destruction caused by magmatic activity during the Mesozoic, the study area has relatively limited remaining Palaeozoic stratigraphic formations.

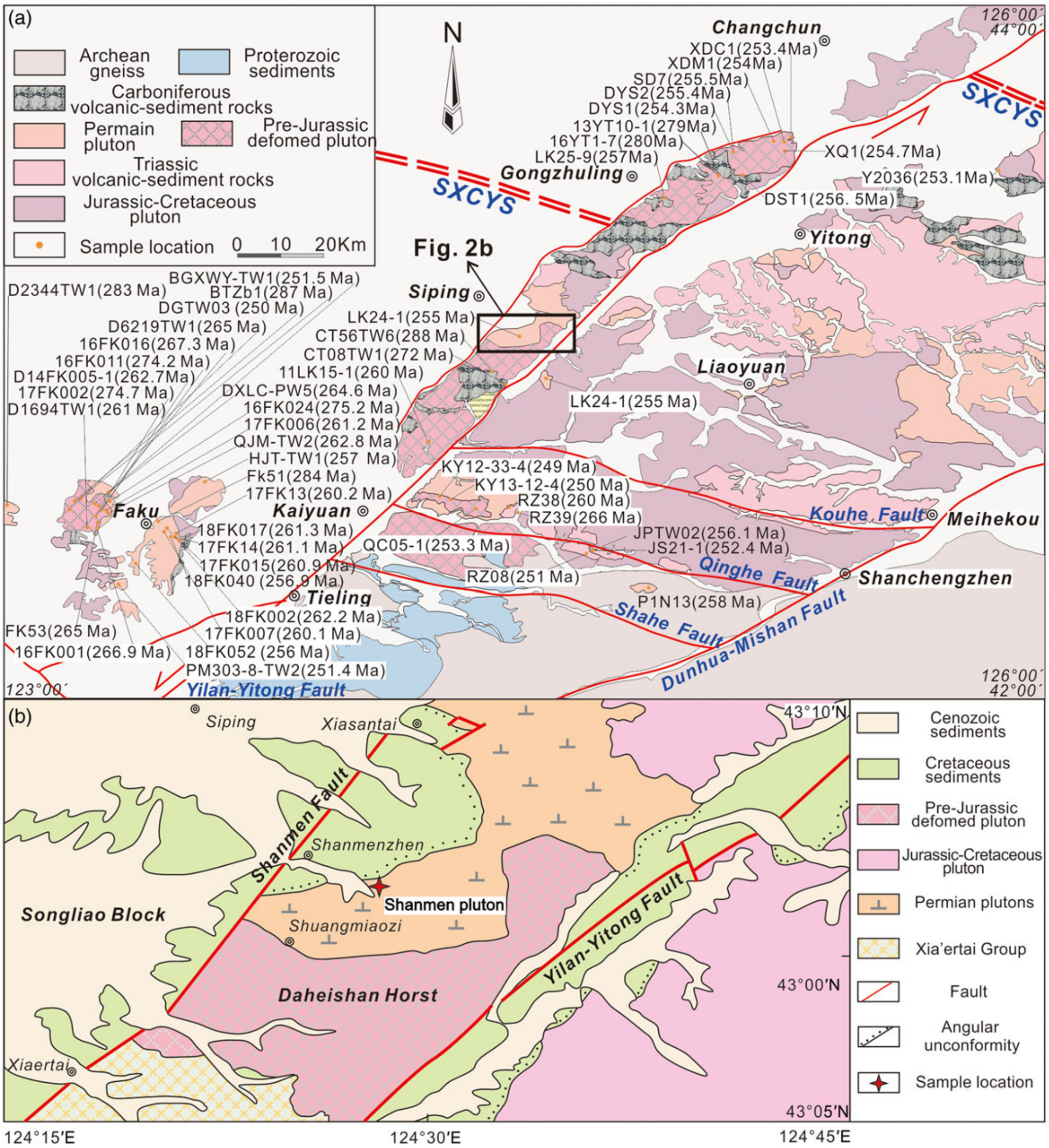


**Figure 2.** (Colour online) (a) Simplified regional geologic map of the Changchun-Kaiyuan showing the distribution of the Permian igneous rocks. All these reported age locations were presented in Table 4; (b) Geological sketch map of the shanmenzhen region, with the sample locations shown. SXCYS: Solonker-Xar Moron-Changchun -Yanji Suture.

In the study area, the intrusive rocks primarily consist of Mesozoic granites and late Paleozoic intrusions (Fig. 2b). The Mesozoic granites mainly comprise Jurassic monzonitic granites and granodiorites. The late Paleozoic intrusive rocks are formed in the Middle Permian, and the lithology includes quartz diorite, syenite granite and granite. Initially, due to the lack of accurate isotope dating data, it was believed that the late Paleozoic intrusions were formed in the Ordovician. However, as the study progressed, 262 ± 2 Ma (Cao, 2013) and 264-260 Ma (this study) were obtained in the study area. In the southern part of the study area, a large area of 'Xia'ertai Group' is distributed, and the overall pattern is spread in a NE direction in a back-shaped pattern (Zhang, 2021). In addition, Mesozoic Cretaceous volcanic sedimentary strata and Cenozoic strata developed in the Songliao Basin (Fig. 2b).

## 3. Field relationships and sample description

### 3.a. Field relationships

The Shanmen pluton in this paper was discovered in the Shanmen Reservoir (124° 28′ 13′′ E, 43° 03′ 20′′ N), which is just ~20 km southeast of Siping. It is mainly composed of quartz diorite, syenite granite and granite. Field observation revealed that the left side of the pluton is a slip fault, with an occurrence of 284/85. Moreover, the mylonitic fine-grained granite intrusions can be observed in the form of veins within the quartz diorite, and both of them underwent metamorphic deformation (Fig. 3a, b).

### 3.b. Petrography

The quartz diorite from SM18-1 is medium-grained with grey-black and composed of plagioclase (70%–80%), quartz (~5%) and biotite (~15%), with minor hornblende (Streckeisen 1976; Fig. 3c).

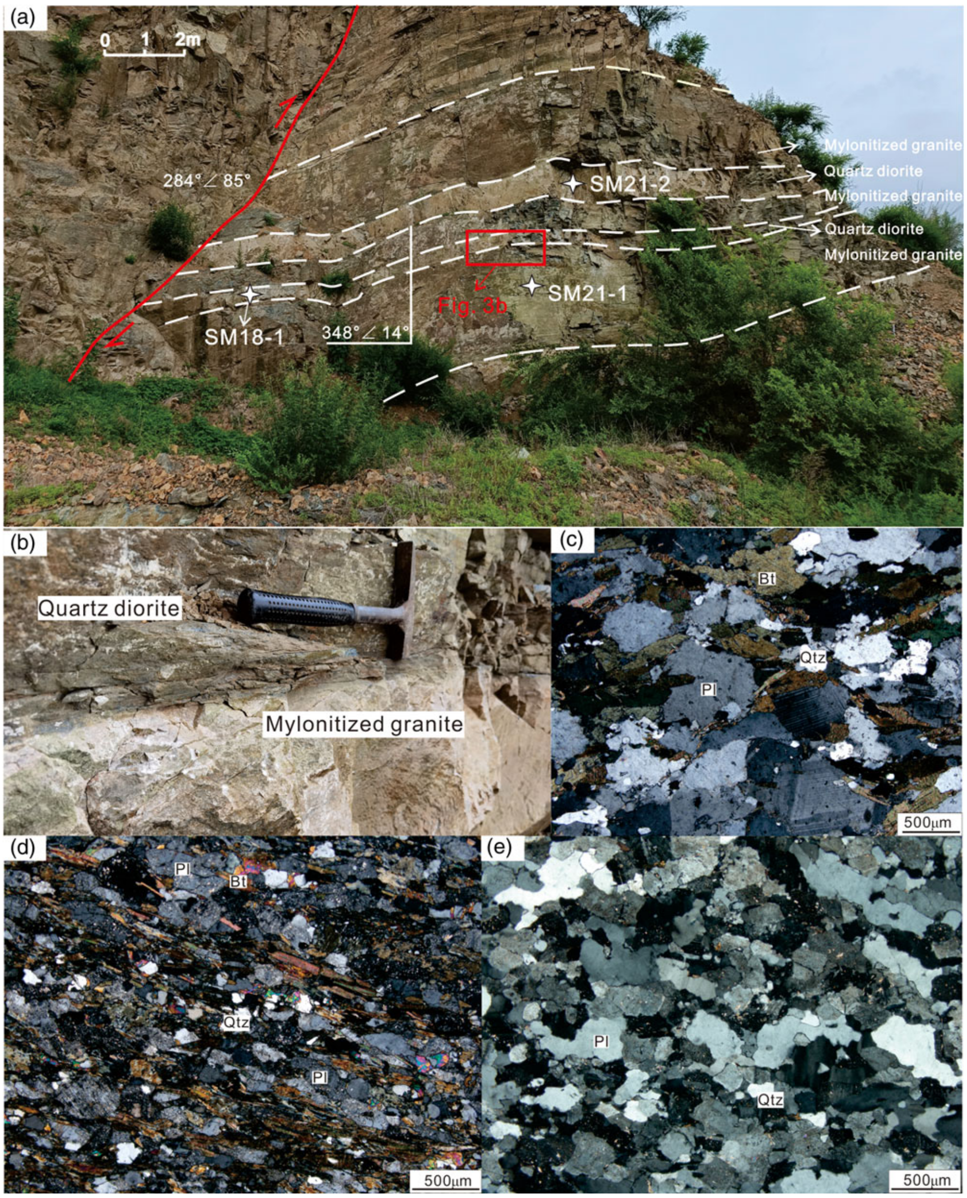


**Figure 3.** (Colour online) (a, b) Field photos of the Shanmen pluton. (c) Microscopic photos for the quartz diorite (SM18-1). (d) Microscopic photos for the quartz diorite (SM21-2). (e) Microscopic photos for the mylonitic granite (SM21-1). Mineral abbreviations: Pl-plagioclase; Bt-biotite; Qtz-quartz.

The quartz diorite from SM21-2 is fine-grained and composed of plagioclase (70%–80%), quartz (~5%) and biotite (~15%) (Streckeisen 1976; Fig. 3d). The deformation of sample SM21-2 is more intense, and the mineral elongation orientation is obvious and more broken.

The mylonitic granite is white-grey with a typical granitic texture and comprises mainly quartz (~30%), plagioclase (~65%) and biotite (< 5 %) (Fig. 3e). Most quartz and feldspar minerals are elongated and oriented.

## 4. Analytical methods

### 4.a. Zircon U-Pb dating

The separation of zircon was performed in the Keda Rock Mineral Separation Company in Langfang City, Hebei Province. The samples were first crushed and then separated using gravitational and magnetic separation methods. Laser ablation inductively coupled plasma mass spectrometry (LA–ICP–MS) U–Pb zircon dating was carried out at the Key Laboratory of Mineral Resources Evaluation in NE Asia, Ministry of Natural Resources, Jilin University, Changchun, China. The correction for common Pb was made following the method of Andersen (2002). The data were processed using the ISOPLOT (Version 3.0) programme (Ludwig, 2003).

### 4.b. Major and trace elements analyses

Major and trace elements were analysed at the premises of ALS Chemex Co. Ltd. in Guangzhou. Major elements were measured by X–ray fluorescence spectrometry from prepared glass discs. Trace elements were instead analysed using ICP–MS after melting the samples at 1025 °C and digesting them using a $HNO_3 + HCL + HF$ mixture.

### 4.c. In situ zircon Hf isotopic analyses

In situ zircon Hf isotopic analyses for sample (SM18-1) were undertaken using a Neptune multi-collector (MC) ICP-MS, equipped with a 193 nm ArF Excimer laser system at the

Tianjin Institute of Geology and Mineral Resources in Tianjin, China. Details of the analytical procedures are described by Wu et al. (2006).

Experiments of in situ Hf isotope ratio analysis for sample (SM21-1, SM21-2) were conducted using a Neptune Plus MC-ICP-MS (Thermo Fisher Scientific, Germany) in combination with a Geolas HD excimer ArF laser ablation system (Coherent, Göttingen, Germany) that was hosted at the Wuhan Sample Solution Analytical Technology Co., Ltd, Hubei, China. Detailed instrument operating conditions and analysis methods can be referred to (Hu *et al.* 2012).

## 5. Results

### 5.a. Zircon U-Pb dating

Samples SM18-1 and SM21-2 were collected from different positions within the Shanmen pluton, as shown in Fig. 3a. The zircon grains are transparent and subhedral with elongation ratios ranging from 1:1 to 2:1. In cathodoluminescence images, most of the grains exhibit oscillatory growth zoning with high Th/U ratios (0.34–1.13), suggesting a magmatic origin (Koschek, 1993; Fig. 4). The zircons show significant depletion of LREE, enrichment of HREE and prominent negative Eu anomalies, which are typical characteristics of magmatic zircons (Belousova *et al.* 2002; Hoskin, 2005; Fig. 5d).

Seventeen zircons from sample SM18-1 give a range of $^{206}Pb/^{238}U$ ages from 267 to 260 Ma (Table 1) and yield a weighted mean age of 263.7 ± 2.7 Ma (MSWD = 0.3, n = 17). This weighted mean age is interpreted as the crystallisation age of the rock (Fig. 5a).

The $^{206}Pb/^{238}U$ ages from 23 analyses for the sample SM21-2 vary from 275 Ma to 256 Ma (Table 1), yielding a weighted mean age of 263.5 ± 1.9 Ma (MSWD = 1.2, n = 23; Fig. 5b), which is interpreted as the crystallisation age of the quartz diorite.

A total of fifteen analytical spots for the sample SM21-1 have $^{206}Pb/^{238}U$ ages varying from 269 to 255 Ma (Table 1), with a weighted mean age of 259.6 ± 1.9 Ma (MSWD = 0.79, n = 15). The age represents the emplacement age of mylonitic granite (Fig. 5c).

### 5.b. Whole-rock geochemical compositions

Table 2 shows the results of analyses of trace and major elements of the representative samples.

The quartz diorite samples have $SiO_2$ = 56.08 wt.% – 61.69 wt.%, $Al_2O_3$ = 16.20 wt.% – 17.08 wt.%, $K_2O$ = 1.37 wt.% – 1.88 wt.%, $Na_2O$ = 4.06 wt.% – 4.55 wt.% and MgO = 2.26 wt.% – 4.37 wt.%, with $Mg^{\#}$ [=100 $Mg^{2+}/(Mg^{2+}+TFe^{2+})$] values of 45 – 56, which indicates that the samples are mostly high-Mg Na-enriched diorite. The samples are classified as medium-K calc-alkaline diorites on the total alkalis versus silica and $K_2O$ vs. $SiO_2$ diagrams (Fig. 6a, b). They exhibit metaluminous affinity, with A/CNK values [molar $Al_2O_3$/ (CaO + $Na_2O$ + $K_2O$)] ranging from 0.82 to 0.93 (Fig. 6c). Moreover, these samples are enriched in LILEs (e.g., Rb, Sr and Ba) and depleted in HFSEs (e.g., Nb, Ta, and Ti) with no negative Eu anomalies (σEu = 0.99 – 1.05; Fig. 7).

The mylonitic granite samples have high $SiO_2$ (73.59 wt% – 75.88 wt%) and $K_2O$ (1.25 wt% – 3.11 wt%) contents, relatively high Sr (272 ppm – 323 ppm), low Y (7.9 ppm – 9.5 ppm) and Yb (0.97 ppm – 1.02 ppm) contents, as well as high Sr/Y ratios of 29 – 40. However, the granite samples have low MgO contents (0.28 wt % – 0.47 wt%) and $Mg^{\#}$ values (28 – 36). These samples belong to the tholeiite and calc-alkaline series (Fig. 6b). On the A/NK vs. A/CNK diagram, A/CNK values of these samples range from 1.02 to 1.04, indicating a peraluminous nature (Fig. 6c). Furthermore, the studied granite samples illustrate strong Eu anomalies (σEu = 0.67 – 0.76; Fig. 7a). In primitive mantle-normalised patterns, these samples involve enrichment in Rb, Ba, Th, K and LREEs and depletion in Nb, Ta, Ti, P and HREEs (Fig. 7b).

### 5.c. In situ zircon Hf isotopic compositions

In situ zircon Hf isotopic compositions of the Shanmen pluton are listed in Table 3. Sixteen analyses of the samples (SM18-1, SM21-2) possess homogeneous initial $^{176}Hf/^{177}Hf$ ratios (0.282777 – 0.282956), with $\varepsilon_{Hf}(t)$ values varying from +5.71 to +12.20 (Fig. 8). Ten zircons from the granite sample (SM21-1) show homogeneous initial $^{176}Hf/^{177}Hf$ ratios (0.282832 – 0.282899), with $\varepsilon_{Hf}(t)$ values ranging from +7.79 to +10.15 (Fig. 8).

## 6. Discussion

### 6.a. Petrogenesis of the Shanmen Pluton

#### 6.a.1. Quartz diorite

The quartz diorites in this paper have $SiO_2$ = 56.08 wt.% – 61.69 wt.%, $Al_2O_3$ = 16.20 wt.% – 17.08 wt.% and MgO = 2.26 wt.% – 4.37 wt.%. Moreover, an obvious characteristic of the quartz diorite is the depletion of Y (11.6 ppm – 16.0 ppm) and Yb (1.00 ppm – 1.62 ppm), enrichment of Sr (819 ppm – 1145 ppm), resulting in high Sr/Y (51.19–90.87) and $(La/Yb)_N$ (7.82–13.62) ratios. These geochemical data suggest that it has the characteristics of adakite, as described by Defant & Drummond (1990). In the $(La/Yb)_N$ vs. $Yb_N$ diagram (Fig. 9a), the samples are plotted in the overlapping range. Conversely, in the Sr/Y vs. Y diagram (Fig. 9b), the samples generally fall within the adakite area. Generally, there are four models to explain the formation of the adakites, as follows: (1) Partial melting of subducting oceanic crust (Defant & Drummond, 1990; Rapp *et al.* 1999); (2) Fractional crystallisation processes of parental basaltic magmas (Defant & Drummond, 1990; Castillo *et al.* 1999); (3) Partial melting of the thickened basaltic lower crust (Kay & Kay, 2002; Xu *et al.* 2002; Xu *et al.* 2006); and (4) Partial melting of the delaminated basaltic lower crust (Kay and Kay, 1993; Xu *et al.* 2002).

Based on the spatial and temporal correlation between adakite and more abundant mafic rocks, a fractional crystallisation model is proposed (Macpherson *et al.* 2006; Jing *et al.* 2022a). However, the scarcity of mafic magmatic rocks and the variable La/Sm and Zr/Sm ratios also reveal that fractional crystallisation is not the primary mechanism, as shown in Fig. 10a, b. The lack of Eu anomalies of the Shanmen adakitic diorites indicates that fractional crystallisation is not the main genetic mechanism of the rocks (Jing *et al.* 2022a; Macpherson *et al.* 2006; Cao *et al.* 2013). Adakites derived from the partial melting of thickened lower crust typically exhibit low Cr, Ni and $Mg^{\#}$ values (< 40). In contrast, the studied quartz diorite demonstrates high-$Mg^{\#}$ values (44.93–55.55), and Cr (30 ppm – 110 ppm) contents indicate that they cannot be formed by the partial melting of the thickened lower crust. In addition, the samples have a high $Na_2O/K_2O$ ratio of 2.37–3.10, which is the characteristic of Na-rich and K-poor. This aligns with the characteristics that they are formed by the partial melting

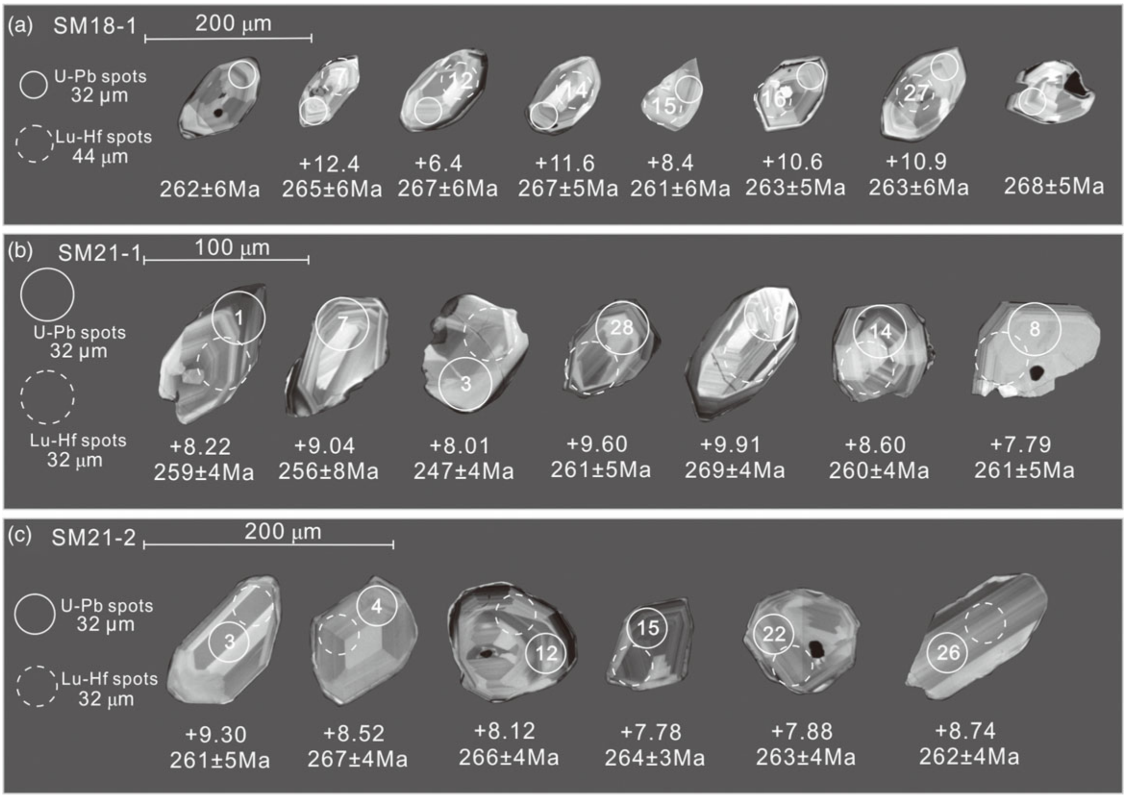


**Figure 4.** (Colour online) Representative cathodoluminescence images of selected zircons of the quartz diorite and mylonitic granite.

of the subducted oceanic crust in an oceanic subduction zone, rather than by the delamination of the basaltic lower crust. (Fig. 9c, d; Defant & Drummond, 1990; Zhang *et al.* 2001; Wang *et al.* 2003, 2006).

The interaction between slab melt and mantle wedge is also an important mechanism for the intermediate rocks with high Mg and Sr/Y ratios (Sen & Dunn, 1994; Kelemen, 1995; Rapp & Watson, 1995; Rapp *et al.* 1999; Wood and Turner, 2009; Jing *et al.* 2022a). In the MgO vs. $SiO_2$ and $SiO_2$ vs. FeO*/ MgO diagrams (Fig. 9e, f), the samples belong to low iron calc-alkaline (LF-CA) Magnesian Andesits, which are similar to the geochemical characteristics of magmatic rocks formed by the interaction of subducted slab and melt-mantle wedge (Deng *et al.* 2009). Furthermore, the zircon $\varepsilon_{Hf}(t)$ values of the quartz diorites recommend that the magma could have originated from metasomatized depleted lower mantle, further supporting this perspective. The above characteristics indicate that the quartz diorite is the product of the interaction between different degrees of slab melt and the overlying mantle wedge.

### 6.a.2. Mylonitic granite

The geochemical characteristics of the granite are consistent with the syenogranite found in the Shanmen region (Cao, 2013). The studied samples exhibit high $SiO_2$ (73.59 wt% – 75.88 wt%), $Al_2O_3$ (12.94 wt% – 13.90 wt%) and $K_2O$ (1.25 wt% – 2.68 wt%), as well as low MgO contents. They also display low $Mg^{\#}$ values and enrich in LREEs and LILEs and deplete in HREEs and HFSEs, which illustrates that our studied granites must have originated from crustal materials (Sun & McDonough, 1989; Rudnick & Gao, 2003). Moreover, the similarities in geochemical characteristics between these granites and I-type granites are further supported by the (Zr + Nb + Ce + Y) vs. TFeO/MgO and Zr vs. 1000*Ga/Al diagrams (Whalen *et al.* 1987; Fig. 10c, d). The zircon εHf(t) values of the granite provide further evidence that the magma originated from the juvenile lower crust. The granite samples demonstrate depletion in Eu anomalies, which is consistent with the partial melting of source rocks with the plagioclase left as a residual mineral. The compelling depletion of Nb, Ta and Ti further confirms that rutile may be another residual mineral (Fig. 7d). Based on these indications, we propose that the granites originated from the partial melting of the intermediate-basic lower crust.

## 6.b. Tectonic implications

### 6.b.1. Diversified sources in the generation of the Permian magmatism

In the eastern CAOB, the northern margin of NCC experienced the subduction of the PAO and the collision of related micro-continental blocks, resulting in widespread Late Paleozoic magmatism. In recent years, numerous Permian magmatic rocks have been discovered in the Changchun-Kaiyuan (Fig. 2a; Table 4). These Permian (ca. 265–250 Ma) rocks mainly consist of high-K calc-alkaline intermediate rocks and granitic intrusions with a metaluminous to weak peraluminous affinity (Fig. 6). The intermediate rocks, including gabbro, gabbro diorite, monzo-diorite, monzonite and quartz diorite, exhibit characteristics of arc magmatic rocks. They are enriched in LILE and LREE, while depleted in HFSE such as Nb, Ta, Ti and HREE (Fig. 7). The

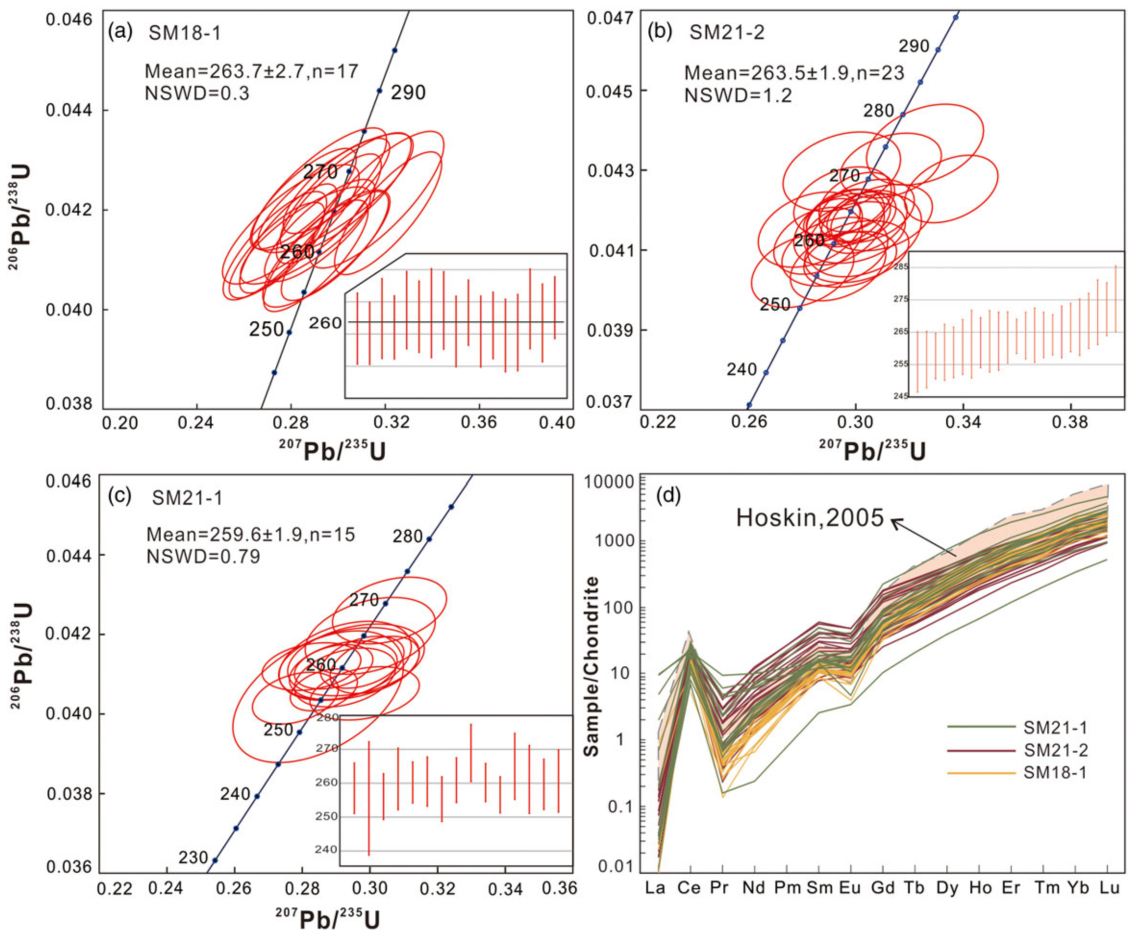


**Figure 5.** (Colour online) (a, b, c) U-Pb concordia diagrams showing zircon ages obtained by LA-ICP-MS. The weighted mean age and MSWD are shown in each figure; (d) chondrite-normalised REE patterns for zircons from the quartz diorite and mylonitic granite.

granitic intrusions consist of syenogranite, monzogranite and granodiorite. Most of them display characteristics of I-type granites, although a small amount illustrates characteristics of A-type granites (Fig. 10c, d). These intrusions are the result of partial melting of crust at different depths and are closely related to the underplating of mantle-derived magma. This study highlights that the quartz diorites and I-type granites together with the Permian magmatism along SXCYS constitute a significant Permian arc magmatic belt. This belt is closely related to the southward subduction of the PAO.

### *6.b.2. Implications for the Middle-Late Permian tectonic evolution of the Solonker-Changchun suture zone*

In general, it is usually difficult for large-scale partial melting of subducted slabs in the oceanic subduction zone (Hernández-Uribe *et al.* 2020; Jing *et al.* 2022a). Our petrogenesis suggests that the adakitic diorite in the Shanmen area most likely originates from partial melting of the subducting oceanic crust, indicating a connection with the tectonic setting associated with the subduction of PAO. There are usually several geodynamic environments for the generation of adakite in the subduction zone: (1) the initiation of subduction; (2) partial melting of young and hot oceanic crust; (3) ridge subduction; and (4) slab break-off (Defant & Drummond, 1990; Sajona *et al.* 1993; Yogodzinski *et al.* 1995; Guivel *et al.* 1999; Calmus *et al.* 2003; Jian *et al.* 2010; Castillo, 2012). The CAOB is usually considered to have undergone prolonged subduction and accretion until the Early-Middle Triassic (Eizenhöfer *et al.* 2014; Eizenhöfer & Zhao, 2018; Li *et al.* 2022b; Xiao *et al.* 2003; Jing *et al.* 2020, 2021; Huang *et al.* 2018; Wu *et al.* 2011). Therefore, the first and second assumptions are not suitable.

The concept of slab windows was originally introduced by Dickinson and Snyder (1979), who associated them with the subduction of obliquely or orthogonally converging oceanic ridges and the process of transforming faults descending into oceanic trenches. The slab break-off can also lead to the slab windows. The upwelling of the asthenospheric mantle through slab windows induces decompression melting, generating mafic melts that interact with the lower crust, leading to the formation of extensive granite. Partial melting of the edge of the subducting slab produces distinctive rock assemblages (Yogodzinski *et al.* 1995). It is worth noting that the upwelling of the asthenosphere often triggers significant extension of the overlying lithosphere, which aligns with the tectonic environment conducive to the formation of A-type granite in the Permian. Recently, the presence of slab windows during the Permian has been proposed in the southwestern and southeastern parts of the CAOB (Windley *et al.* 2007; Yin *et al.* 2010). Numerous ca. 250 Ma adakites, Nb-rich basalts and high-Mg andesites (HMAs) were reported in the Faku-Kaiyuan area,

**Table 1.** LA-ICPMS U-Pb zircon data for the Middle-Late Permain Shanmen pluton

| Analysis point | Element content (ppm) | | | Th/U | Isotope ratio | | | | | | Age/(Ma) | | | | | |
|---|---|---|---|---|---|---|---|---|---|---|---|---|---|---|---|---|
| | Th | U | Pb | | $^{207}Pb/^{206}Pb$ | 1σ | $^{207}Pb/^{235}U$ | 1σ | $^{206}Pb/^{238}U$ | 1σ | $^{207}Pb/^{206}Pb$ | 1σ | $^{207}Pb/^{235}U$ | 1σ | $^{206}Pb/^{238}U$ | 1σ |
| SM18-1 (Diorite) | | | | | | | | | | | | | | | | |
| -01 | 93 | 150 | 8 | 0.62 | 0.0497 | 0.0031 | 0.2788 | 0.0169 | 0.0414 | 0.0009 | 189 | 144 | 250 | 13 | 262 | 6 |
| -03 | 92 | 150 | 8 | 0.61 | 0.0489 | 0.0031 | 0.2739 | 0.0165 | 0.0412 | 0.0008 | 146 | 141 | 246 | 13 | 260 | 5 |
| -07 | 68 | 125 | 7 | 0.55 | 0.0568 | 0.0035 | 0.3212 | 0.0186 | 0.0419 | 0.0010 | 483 | 137 | 283 | 14 | 265 | 6 |
| -08 | 62 | 128 | 7 | 0.49 | 0.0498 | 0.0040 | 0.2861 | 0.0226 | 0.0415 | 0.0008 | 187 | 178 | 255 | 18 | 262 | 5 |
| -09 | 50 | 98 | 5 | 0.52 | 0.0545 | 0.0049 | 0.3032 | 0.0227 | 0.0424 | 0.0010 | 391 | 197 | 269 | 18 | 267 | 6 |
| -10 | 75 | 151 | 8 | 0.50 | 0.0517 | 0.0033 | 0.2960 | 0.0182 | 0.0420 | 0.0009 | 272 | 148 | 263 | 14 | 265 | 6 |
| -11 | 43 | 87 | 4 | 0.50 | 0.0554 | 0.0044 | 0.3162 | 0.0234 | 0.0422 | 0.0011 | 428 | 178 | 279 | 18 | 266 | 7 |
| -12 | 40 | 86 | 4 | 0.46 | 0.0519 | 0.0047 | 0.2989 | 0.0269 | 0.0423 | 0.0010 | 280 | 207 | 266 | 21 | 267 | 6 |
| -13 | 65 | 128 | 6 | 0.51 | 0.0485 | 0.0032 | 0.2731 | 0.0180 | 0.0413 | 0.0009 | 120 | 152 | 245 | 14 | 261 | 5 |
| -14 | 84 | 152 | 8 | 0.56 | 0.0501 | 0.0036 | 0.2852 | 0.0184 | 0.0422 | 0.0008 | 211 | 164 | 255 | 15 | 267 | 5 |
| -15 | 68 | 135 | 7 | 0.50 | 0.0526 | 0.0034 | 0.2986 | 0.0186 | 0.0413 | 0.0009 | 322 | 144 | 265 | 15 | 261 | 6 |
| -16 | 102 | 158 | 9 | 0.65 | 0.0512 | 0.0033 | 0.2922 | 0.0192 | 0.0416 | 0.0008 | 250 | 147 | 260 | 15 | 263 | 5 |
| -22 | 53 | 123 | 6 | 0.43 | 0.0521 | 0.0035 | 0.2905 | 0.0181 | 0.0411 | 0.0009 | 300 | 154 | 259 | 14 | 260 | 6 |
| -24 | 41 | 84 | 4 | 0.49 | 0.0535 | 0.0044 | 0.2950 | 0.0221 | 0.0412 | 0.0010 | 346 | 185 | 262 | 17 | 260 | 6 |
| -25 | 77 | 128 | 7 | 0.60 | 0.0501 | 0.0037 | 0.2919 | 0.0234 | 0.0424 | 0.0010 | 211 | 174 | 260 | 18 | 268 | 6 |
| -27 | 56 | 108 | 5 | 0.52 | 0.0509 | 0.0048 | 0.2799 | 0.0237 | 0.0417 | 0.0010 | 239 | 217 | 251 | 19 | 263 | 6 |
| -30 | 86 | 140 | 8 | 0.62 | 0.0522 | 0.0035 | 0.2992 | 0.0185 | 0.0425 | 0.0008 | 300 | 119 | 266 | 14 | 268 | 5 |
| SM21-2 (Diorite) | | | | | | | | | | | | | | | | |
| -02 | 105 | 132 | 8 | 0.80 | 0.0541 | 0.0028 | 0.3096 | 0.0154 | 0.0418 | 0.0007 | 376 | 117 | 274 | 12 | 264 | 4 |
| -03 | 94 | 97 | 6 | 0.97 | 0.0541 | 0.0034 | 0.3032 | 0.0173 | 0.0414 | 0.0008 | 376 | 144 | 269 | 14 | 261 | 5 |
| -04 | 128 | 167 | 10 | 0.77 | 0.0519 | 0.0032 | 0.2951 | 0.0148 | 0.0422 | 0.0007 | 280 | 143 | 263 | 12 | 267 | 4 |
| -05 | 71 | 105 | 6 | 0.67 | 0.0506 | 0.0033 | 0.2831 | 0.0158 | 0.0415 | 0.0008 | 233 | 144 | 253 | 13 | 262 | 5 |
| -07 | 134 | 132 | 8 | 1.02 | 0.0521 | 0.0030 | 0.2922 | 0.0161 | 0.0410 | 0.0007 | 300 | 133 | 260 | 13 | 259 | 4 |
| -08 | 112 | 162 | 9 | 0.69 | 0.0535 | 0.0027 | 0.3041 | 0.0145 | 0.0420 | 0.0006 | 350 | 115 | 270 | 11 | 265 | 4 |
| -09 | 95 | 142 | 8 | 0.67 | 0.0501 | 0.0031 | 0.2948 | 0.0179 | 0.0430 | 0.0008 | 198 | 147 | 262 | 14 | 271 | 5 |
| -11 | 289 | 280 | 18 | 1.03 | 0.0515 | 0.0021 | 0.2961 | 0.0119 | 0.0418 | 0.0006 | 261 | 91 | 263 | 9 | 264 | 4 |
| -12 | 213 | 312 | 17 | 0.68 | 0.0517 | 0.0019 | 0.3004 | 0.0115 | 0.0422 | 0.0006 | 272 | 92 | 267 | 9 | 266 | 4 |
| -13 | 76 | 111 | 6 | 0.69 | 0.0513 | 0.0032 | 0.2803 | 0.0155 | 0.0405 | 0.0008 | 254 | 143 | 251 | 12 | 256 | 5 |
| -14 | 72 | 125 | 7 | 0.58 | 0.0530 | 0.0029 | 0.2938 | 0.0137 | 0.0415 | 0.0007 | 328 | 129 | 262 | 11 | 262 | 5 |

(*Continued*)

**Table 1.** *(Continued)*

| | | | | | | | | | | | | | | | | |
|---|---|---|---|---|---|---|---|---|---|---|---|---|---|---|---|---|
| -15 | 425 | 473 | 28 | 0.90 | 0.0505 | 0.0015 | 0.2911 | 0.0086 | 0.0418 | 0.0004 | 217 | 70 | 259 | 7 | 264 | 3 |
| -17 | 125 | 165 | 9 | 0.76 | 0.0532 | 0.0027 | 0.2934 | 0.0145 | 0.0406 | 0.0007 | 339 | 115 | 261 | 11 | 257 | 4 |
| -19 | 202 | 181 | 11 | 1.11 | 0.0513 | 0.0027 | 0.2860 | 0.0134 | 0.0412 | 0.0007 | 254 | 120 | 255 | 11 | 260 | 4 |
| -22 | 124 | 192 | 10 | 0.64 | 0.0531 | 0.0025 | 0.3031 | 0.0131 | 0.0417 | 0.0006 | 345 | 103 | 269 | 10 | 263 | 4 |
| -23 | 155 | 178 | 10 | 0.87 | 0.0531 | 0.0027 | 0.2979 | 0.0141 | 0.0408 | 0.0006 | 345 | 119 | 265 | 11 | 258 | 4 |
| -24 | 140 | 142 | 9 | 0.99 | 0.0535 | 0.0030 | 0.3003 | 0.0158 | 0.0410 | 0.0006 | 350 | 128 | 267 | 12 | 259 | 4 |
| -25 | 271 | 242 | 16 | 1.12 | 0.0514 | 0.0021 | 0.2973 | 0.0127 | 0.0418 | 0.0006 | 261 | 96 | 264 | 10 | 264 | 4 |
| -26 | 157 | 161 | 10 | 0.97 | 0.0528 | 0.0028 | 0.2996 | 0.0154 | 0.0414 | 0.0006 | 320 | 122 | 266 | 12 | 262 | 4 |
| -27 | 197 | 269 | 15 | 0.73 | 0.0573 | 0.0025 | 0.3355 | 0.0142 | 0.0425 | 0.0007 | 502 | 94 | 294 | 11 | 268 | 4 |
| -28 | 104 | 138 | 8 | 0.76 | 0.0538 | 0.0027 | 0.3257 | 0.0178 | 0.0436 | 0.0008 | 365 | 108 | 286 | 14 | 275 | 5 |
| -29 | 358 | 432 | 25 | 0.83 | 0.0521 | 0.0018 | 0.3021 | 0.0105 | 0.0418 | 0.0005 | 300 | 80 | 268 | 8 | 264 | 3 |
| -30 | 123 | 199 | 11 | 0.62 | 0.0533 | 0.0028 | 0.3130 | 0.0154 | 0.0431 | 0.0007 | 343 | 120 | 277 | 12 | 272 | 4 |
| | | | | | | | | SM21-1 (Granite) | | | | | | | | |
| -01 | 234 | 472 | 23 | 0.49 | 0.0514 | 0.0020 | 0.2927 | 0.0122 | 0.0409 | 0.0006 | 257 | 91 | 261 | 10 | 259 | 4 |
| -02 | 30.1 | 47.5 | 2 | 0.63 | 0.0549 | 0.0051 | 0.2847 | 0.0206 | 0.0404 | 0.0014 | 406 | 214 | 254 | 16 | 256 | 8 |
| -07 | 102 | 191 | 9 | 0.53 | 0.0533 | 0.0023 | 0.2984 | 0.0132 | 0.0405 | 0.0005 | 339 | 98 | 265 | 10 | 256 | 3 |
| -08 | 44.2 | 85.1 | 4 | 0.52 | 0.0530 | 0.0034 | 0.2959 | 0.0165 | 0.0414 | 0.0007 | 328 | 151 | 263 | 13 | 261 | 5 |
| -13 | 360 | 320 | 18 | 1.13 | 0.0499 | 0.0022 | 0.2827 | 0.0119 | 0.0412 | 0.0005 | 191 | 106 | 253 | 9 | 260 | 3 |
| -14 | 229 | 357 | 19 | 0.64 | 0.0531 | 0.0018 | 0.3014 | 0.0108 | 0.0412 | 0.0006 | 332 | 80 | 267 | 8 | 260 | 4 |
| -15 | 261 | 360 | 18 | 0.73 | 0.0503 | 0.0020 | 0.2780 | 0.0104 | 0.0404 | 0.0005 | 209 | 90 | 249 | 8 | 255 | 3 |
| -17 | 172 | 304 | 15 | 0.57 | 0.0526 | 0.0018 | 0.2977 | 0.0101 | 0.0413 | 0.0005 | 309 | 78 | 265 | 8 | 261 | 3 |
| -18 | 54.7 | 140 | 7 | 0.39 | 0.0536 | 0.0027 | 0.3058 | 0.0138 | 0.0426 | 0.0007 | 354 | 111 | 271 | 11 | 269 | 4 |
| -21 | 250 | 486 | 24 | 0.51 | 0.0509 | 0.0016 | 0.2893 | 0.0095 | 0.0412 | 0.0005 | 235 | 74 | 258 | 7 | 260 | 3 |
| -23 | 455 | 608 | 31 | 0.75 | 0.0510 | 0.0014 | 0.2864 | 0.0081 | 0.0406 | 0.0004 | 243 | 65 | 256 | 6 | 257 | 3 |
| -25 | 57.2 | 168 | 8 | 0.34 | 0.0532 | 0.0030 | 0.3001 | 0.0157 | 0.0420 | 0.0008 | 345 | 125 | 266 | 12 | 265 | 5 |
| -28 | 68.3 | 112 | 6 | 0.61 | 0.0533 | 0.0032 | 0.2927 | 0.0159 | 0.0413 | 0.0008 | 339 | 137 | 261 | 13 | 261 | 5 |
| -29 | 194 | 328 | 16 | 0.59 | 0.0513 | 0.0022 | 0.2921 | 0.0130 | 0.0411 | 0.0006 | 254 | 96 | 260 | 10 | 260 | 4 |
| -30 | 126 | 152 | 8 | 0.82 | 0.0521 | 0.0031 | 0.2938 | 0.0170 | 0.0413 | 0.0007 | 300 | 135 | 262 | 13 | 261 | 5 |

**Table 2.** Major (wt%) and trace (ppm) elements of the Middle-Late Permian Shanmen pluton

| Analysis point | SM18-1-1 | SM18-1-2 | SM21-2A | SM21-2B | SM21-2C | SM21-2D | SM21-2E | SM21-1A | SM21-1B | SM21-1C | SM21-1D | SM21-1E |
|---|---|---|---|---|---|---|---|---|---|---|---|---|
| Rock type | Quartz diorite | | Quartz diorite | | | | | Mylonitized granite | | | | |
| $SiO_2$ | 61.69 | 60.36 | 56.08 | 56.69 | 57.09 | 56.71 | 56.81 | 75.88 | 73.77 | 73.59 | 75.51 | 75.71 |
| $Al_2O_3$ | 16.77 | 16.70 | 17.00 | 16.88 | 16.20 | 16.75 | 17.08 | 12.98 | 13.90 | 13.90 | 13.11 | 12.94 |
| CaO | 4.73 | 4.90 | 6.75 | 6.57 | 5.97 | 5.90 | 6.11 | 1.09 | 1.44 | 1.41 | 0.89 | 0.97 |
| $TFe_2O_3$ | 5.80 | 6.20 | 7.40 | 7.34 | 7.37 | 7.14 | 7.57 | 1.54 | 1.80 | 1.81 | 1.49 | 1.39 |
| $K_2O$ | 1.86 | 1.88 | 1.36 | 1.47 | 1.48 | 1.49 | 1.37 | 1.25 | 2.60 | 2.60 | 3.11 | 2.68 |
| MgO | 2.26 | 2.39 | 4.37 | 4.29 | 3.79 | 4.18 | 4.25 | 0.28 | 0.47 | 0.45 | 0.28 | 0.29 |
| $Na_2O$ | 4.55 | 4.46 | 4.21 | 4.06 | 4.16 | 4.44 | 4.09 | 5.66 | 4.87 | 4.93 | 4.62 | 4.91 |
| $TiO_2$ | 0.74 | 0.80 | 0.97 | 0.89 | 0.87 | 0.89 | 0.90 | 0.16 | 0.24 | 0.24 | 0.17 | 0.16 |
| $P_2O_5$ | 0.20 | 0.22 | 0.25 | 0.26 | 0.25 | 0.26 | 0.25 | 0.03 | 0.06 | 0.06 | 0.03 | 0.02 |
| MnO | 0.12 | 0.12 | 0.15 | 0.15 | 0.14 | 0.14 | 0.13 | 0.02 | 0.02 | 0.02 | 0.02 | 0.02 |
| LOI | 1.11 | 1.48 | 1.73 | 1.75 | 1.96 | 2.61 | 1.53 | 0.79 | 1.06 | 1.22 | 0.87 | 1.00 |
| $Mg^{\#}$ | 45 | 45 | 56 | 55 | 52 | 55 | 54 | 28 | 36 | 34 | 28 | 31 |
| Total | 99.83 | 99.51 | 100.27 | 100.35 | 99.28 | 100.51 | 100.09 | 99.68 | 100.26 | 100.26 | 100.11 | 100.09 |
| Rb | 52.9 | 58.3 | 47.0 | 54.4 | 55.8 | 58.1 | 45.8 | 23.1 | 55.6 | 55.9 | 53.3 | 48.0 |
| Ba | 809 | 734 | 682 | 744 | 668 | 616 | 984 | 516 | 862 | 881 | 1150 | 1090 |
| Th | 4.30 | 3.88 | 4.04 | 3.97 | 3.83 | 3.95 | 4.25 | 16.70 | 8.91 | 9.19 | 17.05 | 16.85 |
| U | 1.40 | 1.29 | 1.24 | 1.28 | 1.23 | 1.32 | 1.24 | 2.06 | 1.55 | 1.33 | 2.13 | 2.08 |
| Nb | 4.5 | 4.5 | 3.7 | 3.4 | 3.5 | 3.6 | 3.6 | 4.5 | 6.5 | 6.5 | 4.7 | 4.5 |
| Ta | 0.5 | 0.4 | 0.2 | 0.2 | 0.2 | 0.2 | 0.2 | 0.6 | 0.6 | 0.6 | 0.6 | 0.6 |
| La | 22.8 | 18.8 | 22.5 | 21.7 | 20.2 | 19.9 | 21.4 | 22.8 | 26.4 | 28.8 | 21.2 | 23.7 |
| Ce | 45.4 | 39.1 | 45.1 | 43.3 | 40.5 | 40.6 | 43.4 | 39.0 | 48.3 | 53.0 | 36.0 | 40.0 |
| Pr | 5.06 | 4.78 | 5.54 | 5.30 | 4.99 | 5.07 | 5.32 | 3.86 | 5.07 | 5.55 | 3.55 | 3.96 |
| Sr | 869 | 819 | 1135 | 1145 | 1115 | 1040 | 1085 | 272 | 285 | 274 | 323 | 295 |
| Nd | 19.3 | 19.1 | 22.9 | 21.7 | 20.4 | 20.7 | 21.8 | 12.4 | 17.0 | 18.8 | 11.4 | 12.6 |
| Zr | 169 | 209 | 136 | 131 | 95 | 107 | 117 | 133 | 172 | 167 | 138 | 132 |
| Hf | 4.2 | 5.2 | 3.3 | 3.2 | 2.5 | 2.7 | 2.9 | 3.8 | 4.5 | 4.4 | 3.9 | 3.8 |
| Sm | 3.76 | 3.94 | 4.50 | 4.18 | 3.93 | 3.99 | 4.17 | 1.87 | 2.72 | 2.99 | 1.72 | 1.92 |
| Eu | 1.21 | 1.26 | 1.34 | 1.31 | 1.20 | 1.26 | 1.24 | 0.40 | 0.60 | 0.63 | 0.39 | 0.38 |
| Gd | 3.10 | 3.40 | 3.61 | 3.25 | 3.15 | 3.17 | 3.25 | 1.42 | 1.98 | 2.12 | 1.33 | 1.44 |
| Tb | 0.47 | 0.52 | 0.51 | 0.45 | 0.43 | 0.45 | 0.46 | 0.22 | 0.30 | 0.31 | 0.21 | 0.21 |
| Dy | 2.67 | 2.88 | 2.80 | 2.56 | 2.38 | 2.45 | 2.49 | 1.31 | 1.67 | 1.73 | 1.26 | 1.34 |
| Y | 15.1 | 16.0 | 13.7 | 12.6 | 11.6 | 12.2 | 12.4 | 7.9 | 9.3 | 9.5 | 8.0 | 8.3 |
| Ho | 0.56 | 0.57 | 0.52 | 0.47 | 0.44 | 0.47 | 0.47 | 0.26 | 0.32 | 0.33 | 0.27 | 0.28 |
| Er | 1.52 | 1.64 | 1.39 | 1.29 | 1.18 | 1.20 | 1.28 | 0.79 | 0.94 | 1.00 | 0.84 | 0.89 |
| Tm | 0.25 | 0.26 | 0.19 | 0.18 | 0.16 | 0.17 | 0.18 | 0.14 | 0.15 | 0.15 | 0.14 | 0.14 |
| Yb | 1.57 | 1.62 | 1.18 | 1.09 | 1.00 | 1.07 | 1.09 | 0.97 | 1.01 | 0.98 | 1.02 | 1.02 |
| Lu | 0.25 | 0.26 | 0.18 | 0.17 | 0.16 | 0.17 | 0.16 | 0.16 | 0.16 | 0.16 | 0.18 | 0.18 |
| ΣREE | 123.02 | 114.13 | 125.96 | 119.55 | 111.72 | 112.87 | 119.11 | 93.5 | 115.92 | 126.05 | 87.51 | 96.36 |
| ΣLREE | 97.53 | 86.98 | 101.88 | 97.49 | 91.22 | 91.52 | 97.33 | 80.33 | 100.09 | 109.77 | 74.26 | 82.56 |
| ΣHREE | 25.49 | 27.15 | 24.08 | 22.06 | 20.50 | 21.35 | 21.78 | 13.17 | 15.83 | 16.28 | 13.25 | 13.80 |
| LREE/HREE | 3.83 | 3.20 | 4.23 | 4.42 | 4.45 | 4.29 | 4.47 | 6.10 | 6.32 | 6.74 | 5.60 | 5.98 |
| $(La/Yb)_N$ | 9.79 | 7.82 | 12.86 | 13.42 | 13.62 | 12.54 | 13.24 | 15.85 | 17.62 | 19.81 | 14.01 | 15.67 |
| δEu | 1.05 | 1.03 | 0.99 | 1.05 | 1.01 | 1.05 | 0.99 | 0.72 | 0.76 | 0.73 | 0.76 | 0.67 |

https://doi.org/10.1017/S001675682300078X Published online by Cambridge University Press

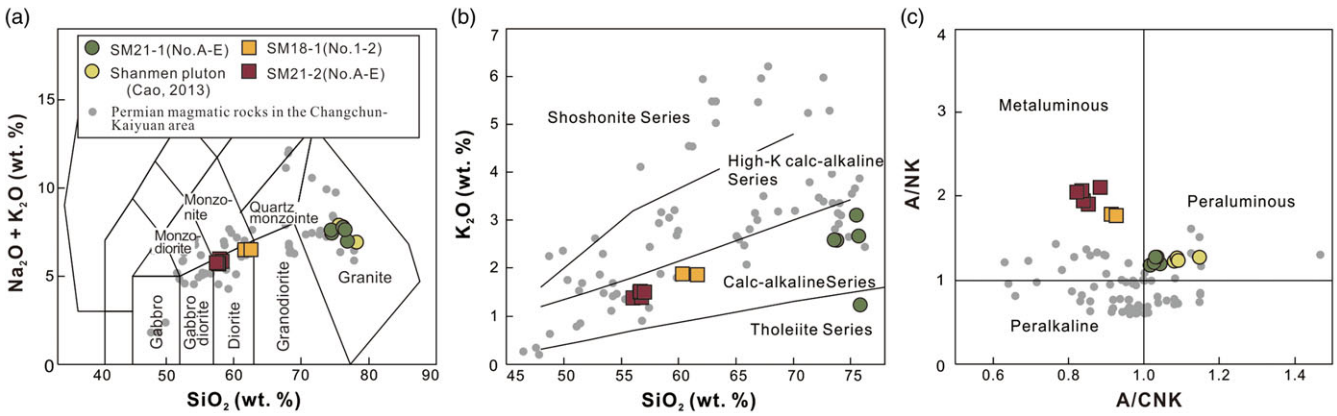


**Figure 6.** (Colour online) Plots of (a) ($Na_2O + K_2O$) vs. $SiO_2$ diagram (TAS; Irvine & Baragar, 1971); (b) $SiO_2$ vs. $K_2O$ diagram (Peccerillo & Taylor, 1976); (c) A/NK [molar ratio $Al_2O_3$/($Na_2O + K_2O$)] vs. A/CNK [molar ratios $Al_2O_3$/ (CaO + Na2O + K2O)] diagram (Maniar & Piccoli, 1989) of the quartz diorite and mylonitic granite. The data of Permian magmatic rocks distributed in the Changchun-Kaiyuan area are from Cao. (2013); Jing et al. (2021); Liu et al. (2020); Song et al. (2018); Shi et al. (2019); and Yuan et al. (2016).

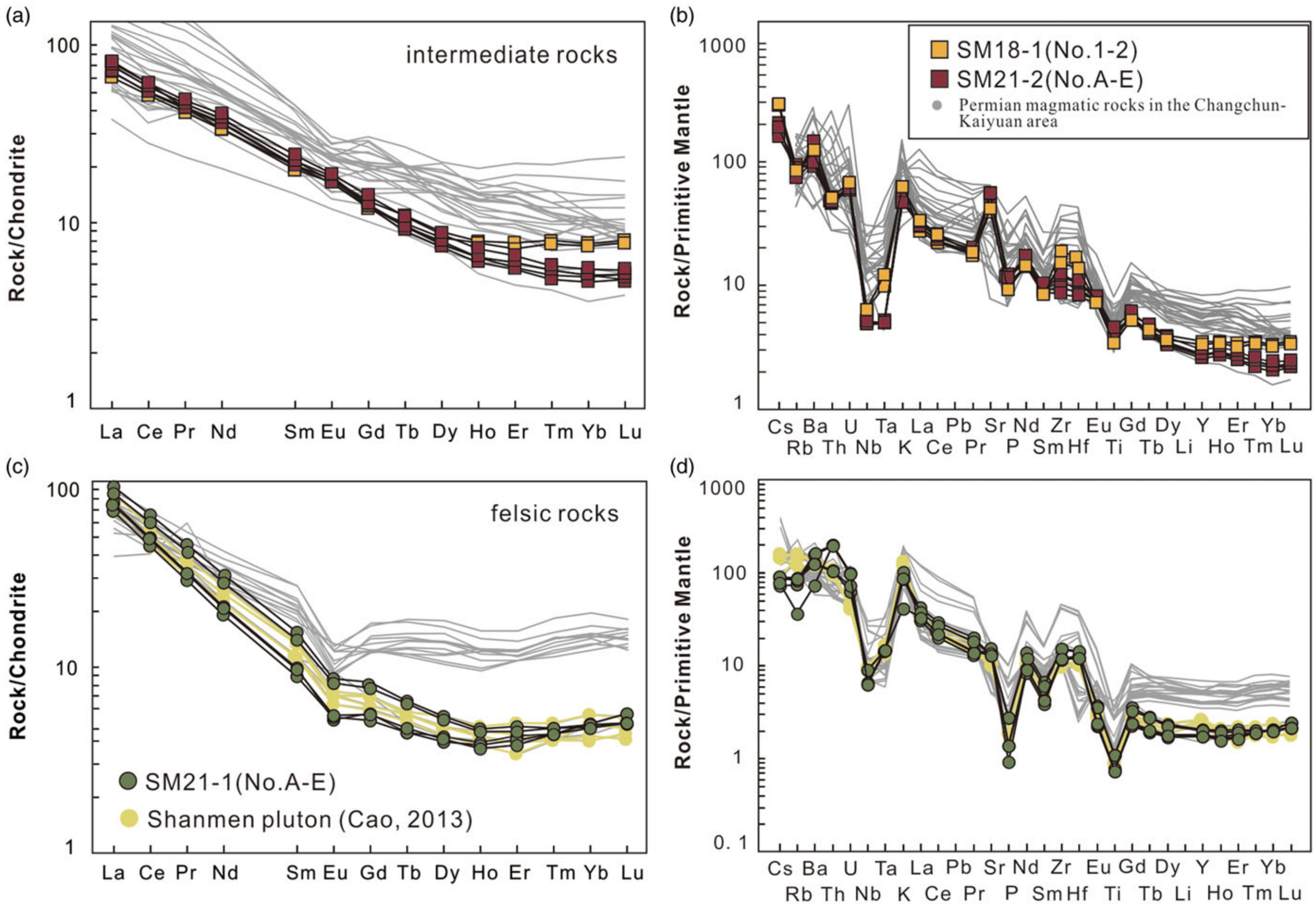


**Figure 7.** (Colour online) Chondrite-normalised REE patterns (a, c; normalisation values from Boynton, 1984) and primitive mantle-normalised trace element spider diagram (b, d; normalisation values from Sun & McDonough, 1989) of the quartz diorite and mylonitic granite.

https://doi.org/10.1017/S001675682300078X Published online by Cambridge University Press

**Table 3.** In situ zircon Hf isotopic compositions for the Middle-Late Permian Shanmen pluton

| Analysis point | Age(Ma) | $^{176}Yb/^{177}Hf$ | $^{176}Lu/^{177}Hf$ | $^{176}Hf/^{177}Hf$ | 2σ | $\varepsilon_{Hf}(t)$ | 2σ | $t_{DM1}$(Ma) | $t_{DM2}$(Ma) | $f_{Lu/Hf}$ |
|---|---|---|---|---|---|---|---|---|---|---|
| SM18-1 (Diorite) | | | | | | | | | | |
| SM18-1-7 | 265 | 0.0302 | 0.0009 | 0.282956 | 0.000033 | 12.2 | | 419 | 613 | −0.97 |
| SM18-1-12 | 267 | 0.0367 | 0.0011 | 0.282796 | 0.000031 | 6.5 | | 648 | 1127 | −0.97 |
| SM18-1-14 | 267 | 0.0390 | 0.0011 | 0.282940 | 0.000027 | 11.6 | | 445 | 667 | −0.97 |
| SM18-1-15 | 261 | 0.0252 | 0.0007 | 0.282851 | 0.000023 | 8.4 | | 565 | 952 | −0.98 |
| SM18-1-16 | 263 | 0.0231 | 0.0007 | 0.282917 | 0.000025 | 10.8 | | 472 | 739 | −0.98 |
| SM18-1-27 | 263 | 0.0393 | 0.0012 | 0.282922 | 0.000029 | 10.9 | | 471 | 730 | −0.96 |
| SM21-2 (Diorite) | | | | | | | | | | |
| SM21-2-03 | 261 | 0.031506 | 0.001024 | 0.282878 | 0.000040 | 9.30 | 1.40 | 531 | 694 | −0.97 |
| SM21-2-04 | 267 | 0.025910 | 0.000885 | 0.282851 | 0.000035 | 8.52 | 1.22 | 567 | 749 | −0.97 |
| SM21-2-05 | 262 | 0.024083 | 0.000809 | 0.282845 | 0.000039 | 8.19 | 1.35 | 575 | 766 | −0.98 |
| SM21-2-12 | 266 | 0.018165 | 0.000688 | 0.282840 | 0.000035 | 8.12 | 1.22 | 580 | 774 | −0.98 |
| SM21-2-15 | 264 | 0.031471 | 0.001099 | 0.282833 | 0.000033 | 7.78 | 1.16 | 596 | 794 | −0.97 |
| SM21-2-19 | 260 | 0.032500 | 0.001049 | 0.282777 | 0.000041 | 5.71 | 1.44 | 674 | 923 | −0.97 |
| SM21-2-22 | 263 | 0.016092 | 0.000556 | 0.282834 | 0.000038 | 7.88 | 1.32 | 586 | 787 | −0.98 |
| SM21-2-25 | 264 | 0.040888 | 0.001290 | 0.282823 | 0.000040 | 7.39 | 1.40 | 613 | 819 | −0.96 |
| SM21-2-26 | 262 | 0.031636 | 0.001013 | 0.282861 | 0.000040 | 8.74 | 1.41 | 555 | 731 | −0.97 |
| SM21-2-29 | 264 | 0.017473 | 0.000637 | 0.282868 | 0.000042 | 9.09 | 1.48 | 540 | 710 | −0.98 |
| SM21-1 (Granite) | | | | | | | | | | |
| SM21-1-01 | 259 | 0.037990 | 0.001319 | 0.282850 | 0.000038 | 8.22 | 1.33 | 576 | 762 | −0.96 |
| SM21-1-02 | 256 | 0.032170 | 0.001139 | 0.282874 | 0.000040 | 9.04 | 1.39 | 538 | 707 | −0.97 |
| SM21-1-03 | 247 | 0.020177 | 0.000695 | 0.282848 | 0.000035 | 8.01 | 1.24 | 568 | 766 | −0.98 |
| SM21-1-08 | 261 | 0.009760 | 0.000369 | 0.282832 | 0.000036 | 7.79 | 1.25 | 586 | 791 | −0.99 |
| SM21-1-14 | 260 | 0.042496 | 0.001580 | 0.282861 | 0.000040 | 8.60 | 1.41 | 563 | 739 | −0.95 |
| SM21-1-15 | 255 | 0.033407 | 0.001159 | 0.282845 | 0.000038 | 7.97 | 1.33 | 581 | 775 | −0.97 |
| SM21-1-18 | 269 | 0.038162 | 0.001276 | 0.282891 | 0.000035 | 9.91 | 1.21 | 515 | 661 | −0.96 |
| SM21-1-25 | 265 | 0.024165 | 0.000845 | 0.282899 | 0.000039 | 10.15 | 1.35 | 499 | 642 | −0.97 |
| SM21-1-28 | 261 | 0.039219 | 0.001313 | 0.282888 | 0.000037 | 9.60 | 1.28 | 521 | 675 | −0.96 |
| SM21-1-30 | 261 | 0.025098 | 0.000858 | 0.282845 | 0.000038 | 8.18 | 1.33 | 575 | 766 | −0.97 |

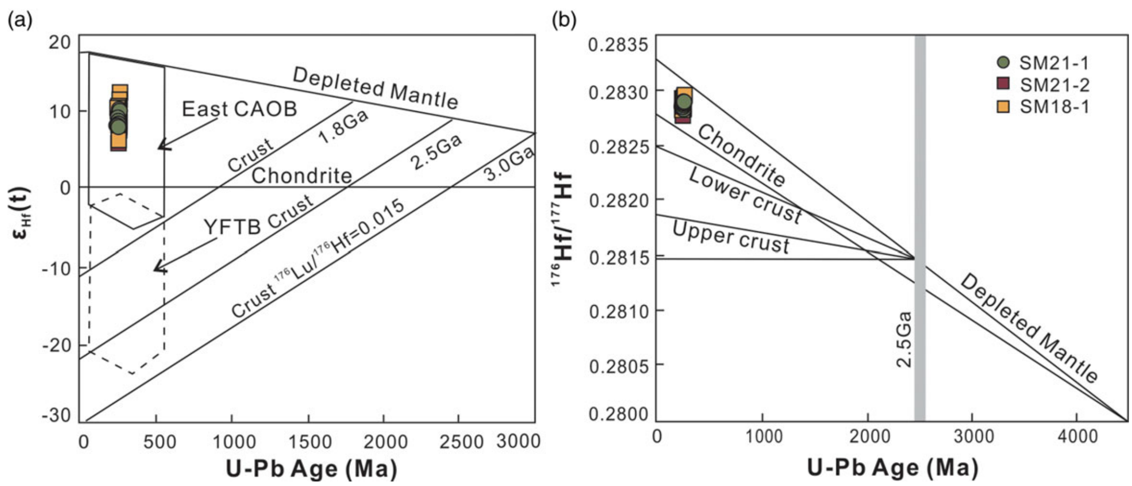


**Figure 8.** (Colour online) Plot of zircon $\varepsilon_{Hf}(t)$ vs. U/Pb age. Shaded areas represent the granitoid from the east CAOB and YFTB (data from Yang et al. 2006; Wu et al. 2007b). CAOB = the Central Asian Orogenic Belt; YFTB = Yanshan Fold-and-Thrust Belt.

https://doi.org/10.1017/S001675682300078X Published online by Cambridge University Press

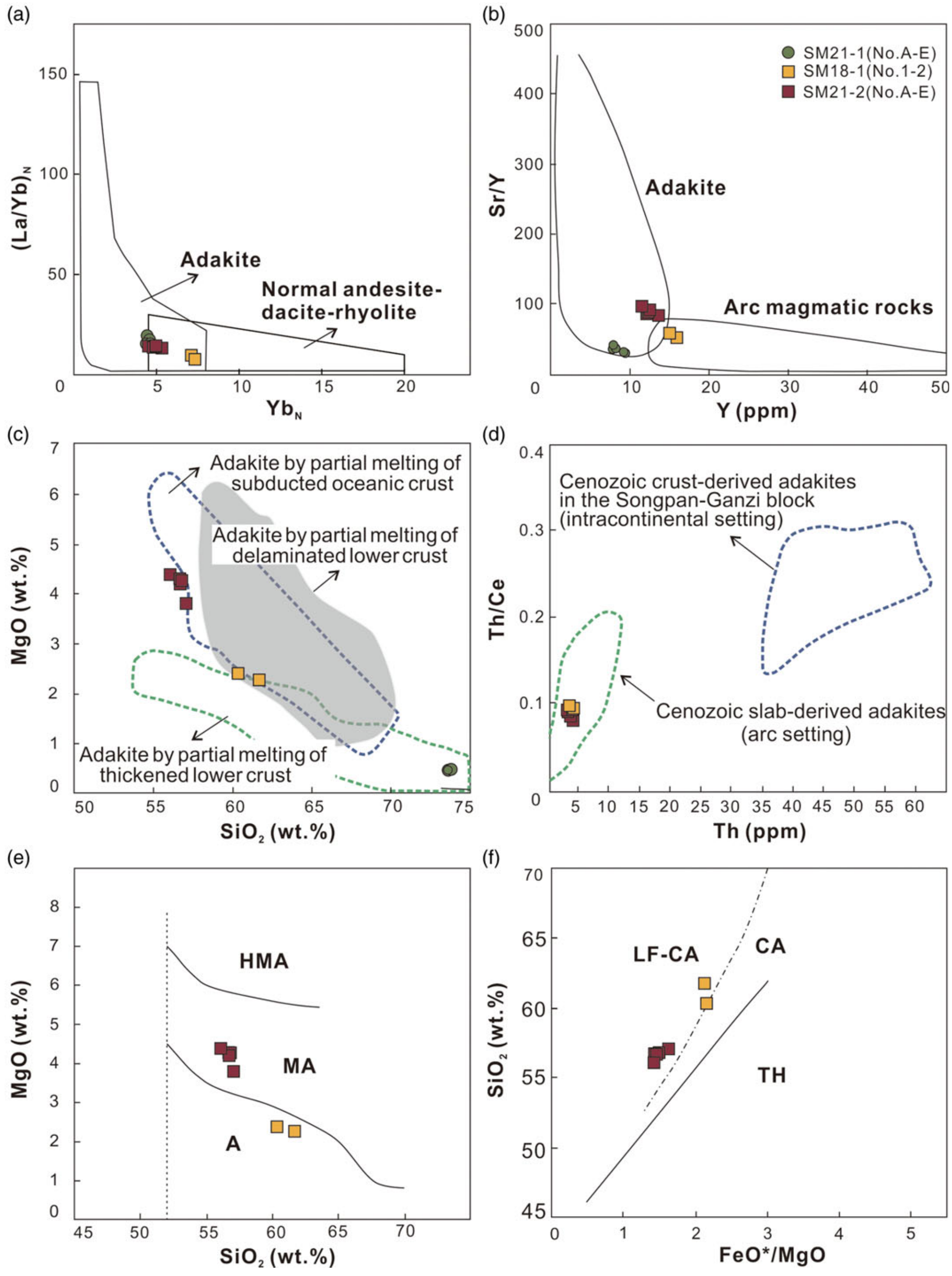


**Figure 9.** (Colour online) (a) $(La/Yb)_N$ vs. $Yb_N$ diagram (Defant &Drummond, 1990); (b) Sr/Y vs. Y diagram (Defant & Drummond, 1990); (c) $SiO_2$ vs. MgO diagram; (d) Th vs. Th/Ce; (e) MgO vs. $SiO_2$ diagram (blue and grey region from Wang et al, 2006); and (f) $SiO_2$ vs. FeO*/MgO diagram (Jing *et al.* 2022a) of the quartz diorite and mylonitic granite. HMA: High-Mg andesites, MA: Mg andesites; LF-CA: low iron calc-alkaline series; CA: calc-alkaline series; TH: tholeiitic series.

further clarifying the existence of slab windows (Yuan *et al.* 2016; Liu *et al.* 2020; Jing *et al.* 2022a).

Along the SXCYS, there is an east-west trending belt of Permian arc magmatic belt and Late Permian-Early Triassic high-Mg andesites (Yuan *et al.* 2016; Liu *et al.* 2012; Li *et al.* 2007; Shen *et al.* 2020; Fu *et al.* 2010). This belt roughly parallels the SXCYS. Although the subduction of the mid-ocean ridge parallel to the trench can also explain this belt, most of the mid-ocean ridges and subduction zones are oblique or orthogonal. Additionally, there was no regional metamorphism of high temperature and low pressure during the Late Permian to the Early-Middle Triassic in the study area. Based on the evidence, we propose that the formation of the Shanmen pluton can be attributed to the upwelling of hot asthenospheric, which is closely connected to the slab break-off mechanism (Fig. 11).

## 7. Conclusions

1. LA-ICP-MS zircon U-Pb dating indicates the Shanmen pluton in the eastern part of the CAOB emplaced in the Middle-Late Permian (263–259 Ma).
2. The quartz diorite is the product of the interaction between different degrees of slab melt and the overlying mantle wedge.

https://doi.org/10.1017/S001675682300078X Published online by Cambridge University Press

**Table 4.** Reported geochronological data for the Permian magmatic rocks in the Changchun-Kaiyuan area

| Order | GPS location | | Sample | Lithology | Age (Ma) | Method | References |
|---|---|---|---|---|---|---|---|
| 1 | E124°13′06″ | N42°43′47″ | 11LK15-1 | Gabbro | 260±5 | LA–ICPMS | Cao, 2013 |
| 2 | E124°29′33″ | N43°02′32″ | 11LK24-1 | Syenite granite | 262±2 | LA–ICPMS | Cao, 2013 |
| 3 | E124°54′02″ | N43°26′37″ | LK25-9 | Olivine gabbro | 257±2 | SIMS | Cao, 2013 |
| 4 | E124°34′18″ | N42°55′23″ | LK24-1 | Granodiorite | 255±2 | LA–ICPMS | Cao, 2013 |
| 5 | E125°51′59″ | N43°31′32″ | Y2036 | Quartzdiorite | 253.1±0.83 | LA–ICPMS | Chen, 2021 |
| 6 | E124°51′43″ | N42°19′14″ | P1N13 | Schist | 258±5.5 | LA–ICPMS | Guan, 2018 |
| 7 | E123°16′16.1″ | N42°29′36.8″ | 16FK001 | Andesite | 266.9±3.5 | LA–ICPMS | Jing *et al.* 2020 |
| 8 | E123°15′42″ | N42°32′26″ | 16FK016 | Andesite | 267.3±0.9 | LA–ICPMS | Jing *et al.* 2020 |
| 9 | E123°16′2.8″ | N42°31′48.1″ | 16FK011 | Dacite | 274.2±2.2 | LA–ICPMS | Jing *et al.* 2020 |
| 10 | E123°18′22″ | N42°33′46″ | 16FK024 | Rhyolite | 275.2±1.9 | LA–ICPMS | Jing *et al.* 2020 |
| 11 | E123°15′23″ | N42°31′29″ | 17FK002 | Rhyolite | 274.7±1.7 | LA–ICPMS | Jing *et al.* 2020 |
| 12 | E123°17′50.4″ | N42°32′21.3″ | 17FK006 | Monzogranite | 261.2±1.1 | LA–ICPMS | Jing *et al.* 2021 |
| 13 | E123°26′39.4″ | N42°29′16.7″ | 17FK007 | Syengranite | 260.1±0.7 | LA–ICPMS | Jing *et al.* 2021 |
| 14 | E123°29′18.8″ | N42°28′20.2″ | 17FK015 | Monzogranite | 260.9±0.6 | LA–ICPMS | Jing *et al.* 2021 |
| 15 | E123°16′02.8″ | N42°31′48.1″ | D14FK005–1 | Monzogranite | 262.7±1.7 | LA–ICPMS | Jing *et al.* 2021 |
| 16 | E123°27′20.1″ | N42°29′29.6″ | 18FK002 | Syengranite | 262.2±2.8 | LA–ICPMS | Jing *et al.* 2021 |
| 17 | E123°28′38.2″ | N42°28′19.1″ | 18FK040 | Syengranite | 256.9±1.5 | LA–ICPMS | Jing *et al.* 2021 |
| 18 | E123°22′40.9″ | N42°23′26.9″ | 18FK052 | Monzogranite | 256±3.2 | LA–ICPMS | Jing *et al.* 2021 |
| 19 | Faku | | 18FK020-1 | Gabbroic diorite | 251.8±1.6 | LA–ICPMS | Jing *et al.* 2022a |
| 20 | E123°29′44.3″ | N42°28′39.7″ | 17FK13 | Gabbro | 260.2±1.6 | LA–ICPMS | Jing *et al.* 2022b |
| 21 | E123°29′18.8″ | N42°28′20.2″ | 17FK14 | Diorite | 261.1±0.8 | LA–ICPMS | Jing *et al.* 2022b |
| 22 | E123°30′1.50″ | N42°27′26.78″ | 18FK017 | Quartzdiorite | 261.3±2.5 | LA–ICPMS | Jing *et al.* 2022b |
| 23 | E124°28′50″ | N42°32′12″ | RZ39 | Gabbro-diorite | 266±2 | LA–ICPMS | Liu *et al.* 2020 |
| 24 | E124°27′15″ | N42°33′16″ | RZ38 | Monzodiorite | 260±2 | LA–ICPMS | Liu *et al.* 2020 |
| 25 | E124°40′40″ | N42°25′10″ | RZ08 | Monzonitic granite | 251±1.3 | LA–ICPMS | Liu *et al.* 2020 |
| 26 | E125°06′4.6″ | N43°34′33.3″ | DYS1 | Rhyolitic dacite | 254.3±2.5 | LA–ICPMS | Song *et al.* 2018 |
| 27 | E125°06′4.6″ | N43°34′33.3″ | DYS2 | Rhyolitic dacite | 255.4±4.2 | LA–ICPMS | Song *et al.* 2018 |
| 28 | E125°13′22.4″ | N43°36′37.1″ | SD7 | Andesite | 255.5±3 | LA–ICPMS | Song *et al.* 2018 |
| 29 | E125°14′58.1″ | N43°34′49″ | XQ1 | Rhyolite | 254.7±2.6 | LA–ICPMS | Song *et al.* 2018 |
| 30 | E125°16′14.6″ | N43°37′10.1″ | XDC1 | Basaltic lava | 253.4±4.5 | LA–ICPMS | Song *et al.* 2018 |
| 31 | E125°15′0.2″ | N43°36′32.3″ | XDM1 | Andesite | 254±3.6 | LA–ICPMS | Song *et al.* 2018 |
| 32 | E125°07′36.9″ | N43°30′31.6″ | DST1 | Syenite granite | 256.5±3.3 | LA–ICPMS | Song *et al.* 2018 |
| 33 | E123°00′20″ | N42°33′06″ | D2344TW1 | Monzonitic granite | 283±2 | LA–ICPMS | Shi *et al.* 2019 |
| 34 | E123°11′26″ | N42°34′21″ | DGTW03 | Granodiorite mylonite | 250±3 | SHRIMP | Shi *et al.* 2019 |
| 35 | E123°10′45″ | N42°29′41″ | D6219TW1 | Granite | 265±1.2 | LA–ICPMS | Shi *et al.* 2019 |
| 36 | E123°14′49″ | N42°29′51″ | D1694TW1 | Granite | 261±1.9 | LA–ICPMS | Shi *et al.* 2019 |
| 37 | E123°17′41″ | N42°35′33″ | DXLC-PW5 | Granite | 264.6±5.9 | LA–ICPMS | Shi *et al.* 2020 |
| 38 | E123°18′12″ | N42°32′01″ | QJM-TW2 | Granite | 262.8±3.5 | LA–ICPMS | Shi *et al.* 2020 |
| 39 | E123°34′40″ | N42°38′42″ | HJT-TW1 | Granite | 257±3.1 | LA–ICPMS | Shi *et al.* 2020 |
| 40 | E123°15′30″ | N42°33′15″ | BGXWY-TW1 | Basaltic andesite | 251.5±2.1 | LA–ICPMS | Shi *et al.* 2022 |

(*Continued*)

**Table 4.** (*Continued*)

| Order | GPS location | | Sample | Lithology | Age (Ma) | Method | References |
|---|---|---|---|---|---|---|---|
| 41 | E123°19′5.5″ | N42°19′51.5″ | PM303-8-TW2 | Diorite | 251.4±1.6 | LA–ICPMS | Shi *et al.* 2022 |
| 42 | E123°13′01″ | N42°34′40″ | BTZb1 | Andesite | 287±2 | LA–ICPMS | Xue, 2021 |
| 43 | E124°21′36″ | N42°32′40″ | QC05-1 | Andesite | 253.3±3.7 | LA–ICPMS | Xue, 2021 |
| 44 | E124°17′31″ | N42°34′25″ | KY13-12-4 | High-Mg andesite | 250±4 | SIMS | Yuan *et al.* 2016 |
| 45 | E124°15′24″ | N42°34′57″ | KY12-33-4 | High-Mg andesite | ca.249 | SIMS | Yuan *et al.* 2016 |
| 46 | E124°24′06″ | N42°56′32″ | CT56TW6 | Schist | 288±7 | LA–ICPMS | Zhang, 2021 |
| 47 | E124°26′38″ | N42°54′38″ | CT08TW1 | Schist | 272±2 | LA–ICPMS | Zhang, 2021 |
| 48 | E123°15′75″ | N42°29′82″ | FK53 | Granodiorite | 265±4 | SHRIMP | Zhang *et al.* 2005 |
| 49 | E123°25′89″ | N42°30′22″ | FK51 | Granodiorite | 284±3 | SHRIMP | Zhang *et al.* 2005 |
| 50 | Faku | | FK04-19 | Monzodiorite | 261±2 | SHRIMP | Zhang *et al.* 2010 |
| 51 | E124°41′40″ | N42°25′48″ | JPTW02 | Rhyolite | 256.1±1.5 | LA–ICPMS | Zhang *et al.* 2022 |
| 52 | E124°41′40″ | N42°25′48″ | JS21-1 | Rhyolite | 252.4±1.7 | LA–ICPMS | Zhang *et al.* 2022 |
| 53 | E125°03′54″ | N43°30′27″ | 13YT10-1 | Basaltic andesite | 279±1 | LA–ICPMS | Zhou *et al.* 2018 |
| 54 | E125°03′54″ | N43°30′27″ | 16YT1-7 | Andesite | 280±1 | LA–ICPMS | Zhou *et al.* 2018 |

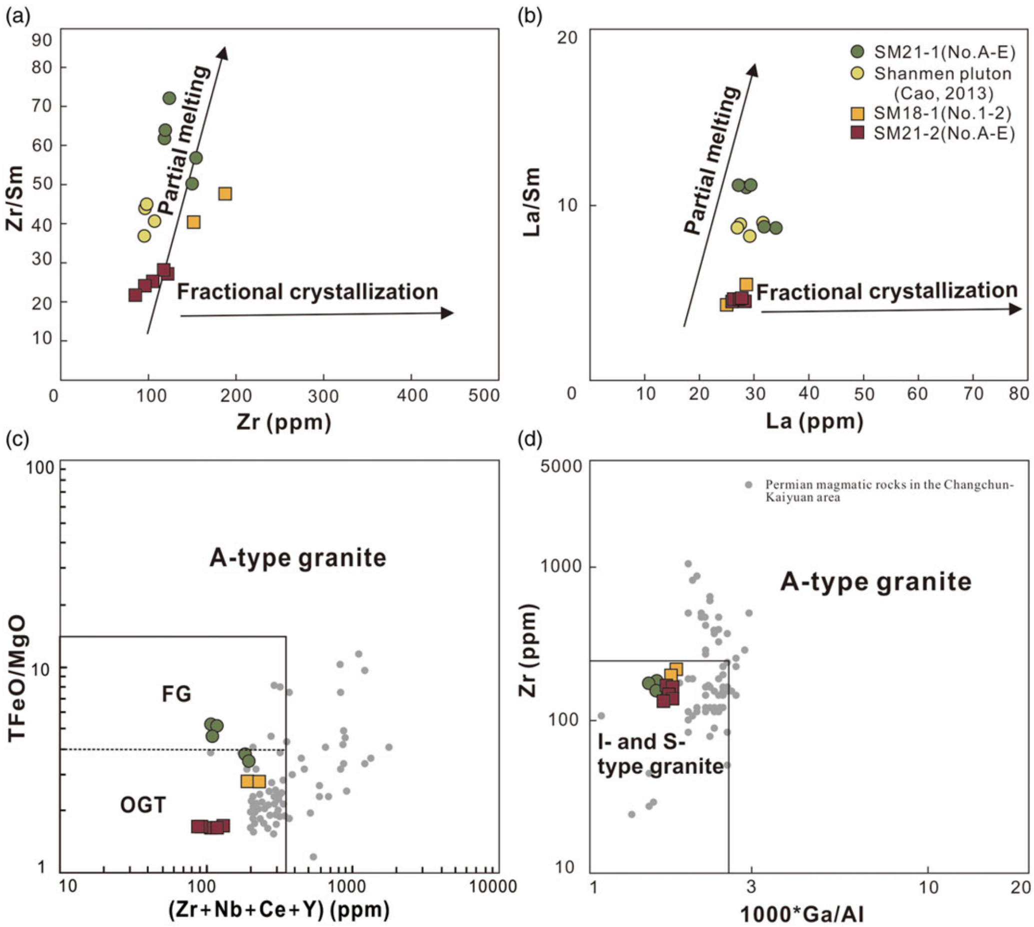


**Figure 10.** (Colour online) (a) Zr/Sm vs. Zr diagram; (b) La/ Sm vs. La diagram (Allègre & Minster, 1978); (c) TFeO/MgO vs. (Zr + Nb + Ce + Y) diagram; and (d) Zr vs. 1000*Ga/Al diagram. FG: fractionated M-, I-, and S-type granite; OTG: unfractionated M-, I- and S-type granite.

https://doi.org/10.1017/S001675682300078X Published online by Cambridge University Press

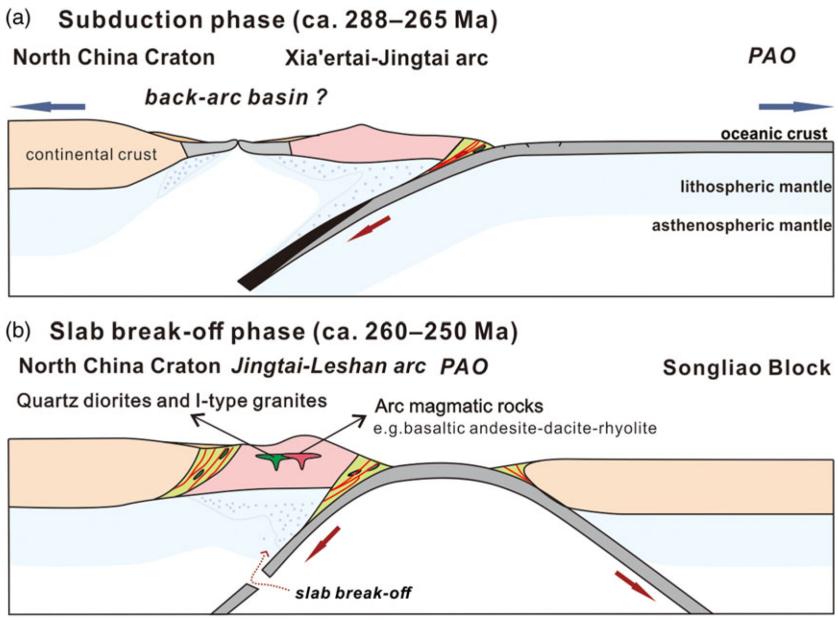


**Figure 11.** (Colour online) Schematic models show the geodynamic evolution of the eastern Palaeo-Asian Ocean during the Permian.

3. The mylonitic granite is veined exposed in diorite, representing the product of partial melting of the intermediate-basic lower crust.
4. The Shanmen pluton formed in an active continental margin setting, in response to southward subduction of the PAO, which is closely linked to the slab break-off mechanism.

**Acknowledgements.** We gratefully acknowledge the constructive suggestions and comments by Prof. Peter Clift and two anonymous reviewers who helped improve the manuscript. We are also sincerely grateful to the Institute of Geology and Mineral Resources in Tianjin, China, and the Wuhan Sample Solution Analytical Technology Co., Ltd, Wuhan, China, during the zircon Lu-Hf isotope analyses. We also thank the staff of the ALS Minerals-ALS Chemex (Guangzhou, China) for their help in major and trace elements analytical works.

**Financial support.** This work was financially supported by the Natural Science Foundation of China (41872203) and the Graduate Innovation Fund of Jilin University (2022101 and 2023CX103).

**Competing interests.** The authors declare that they have no known competing financial interests or personal relationships that could have appeared to influence the work reported in this paper.

## References

**Allègre CJ, Minster JF** (1978) Quantitative models of trace element behavior in magmatic processes. *Earth and Planetary Science Letters* **38**, 1–25.
**Andersen T** (2002) Correction of common lead in U-Pb analyses that do not report 204Pb. *Chemical Geology* **192**, 59–79.
**Belousova E A, Griffin WL, O'Reilly SY and Fisher NI** (2002) Igneous zircon: trace element composition as an indicator of source rock type. *Contributions to Mineralogy and Petrology* **143**, 602–622.
**Boynton WV** (1984) Geochemistry of the rare earth elements: Meteorite studies. *Developments in Geochemistry* **2**, 63–114.
**Calmus T, Aguillon-Robles A, Maury RC, Bellon H, Benoit M, Cotton J, Bourgois J and Michaud F** (2003) Spatial and temporal evolution of basalts and magnesian andesites (bajaites) from Baja California, Mexico: the role of slab melts. *Lithos* **66**, 77–105.
**Cao HH** (2013) Geochronology and Geochemistry of the Late Paleozoic-Early Mesozoic igneous rocks in the eastern segment of the northern margin of the North China Block: PhD thesis, Jilin University, Changchun. 1–158 (in Chinese).
**Cao HH, Xu WL, Pei FP, Wang ZW, Wang F and Wang ZJ** (2013) Zircon U–Pb geochronology and petrogenesis of the Late Paleozoic–Early Mesozoic intrusive rocks in the eastern segment of the northern margin of the North China Block. *Lithos* **170–171**, 191–207.
**Castillo PR** (2012) Adakite petrogenesis. *Lithos* **134–135**, 304–316.
**Castillo PR and Janney PE** (1999) Petrology and geochemistry of Camiguin Island, southern Philippines: Insights to the source of adakites and other lavas in a complex arc setting. *Contributions to Mineralogy and Petrology* **134**, 33.
**Chen B** (2021) Petrogenesis and its Tectonic significance of the Late Permian diorite in central Jilin province: [Dissertation]. Jilin University, Changchun. 1–41 (in Chinese).
**Crameri F, Magni V, Domeier M, Shephard GE, Chotalia K, Cooper G, Eakin CM, Grima AG, Gürer D, Király Á, Mulyukova E, Peters K, Robert B and Thielmann, M** (2020) A transdisciplinary and community–driven database to unravel subduction zone initiation. *Nature Communications* **11**, 3750.
**Defant MJ and Drummond MS** (1990) Derivation of some modern arc magmas by melting of young subducted lithosphere. *Nature* **347**, 662–665.
**Deng JF, Flower MFJ, Liu C, Mo XX, Su SG and Wu ZX** (2009) Nomenclature, diagnosis and origin of High-Magnesian Andesits (HMA) and Magnesian Andesits (MA): A review from petrographic and experimental data. *Geochimica Et Cosmochimica Acta* **73**, A279.
**Dickinson WR, Snyder WS** (1979) Geometry of subducted slabs related to San Andreas transform. *Journal of Geology* **87**, 609–627.
**Eizenhöfer PR and Zhao G** (2018) Solonker Suture in East Asia and its bearing on the final closure of the eastern segment of the Palaeo-Asian Ocean. *Earth Science Review* **186**, 153–172.
**Eizenhöfer PR, Zhao G, Zhang J and Sun M** (2014) Final closure of the Paleo-Asian Ocean along the Solonker Suture Zone: constraints from geochronological and geochemical data of Permian volcanic and sedimentary rocks. *Tectonics* **33**, 441–463.
**Fu CL, Sun DY, Zhang XZ, Wei HY and Gou J** (2010) Discovery and geological significance of the Triassic high-Mg diorites in Hunchu area, Jilin Province. *Acta Petrologica Sinica* **26**, 1089–1102 (in Chinese with English abstract).
**Guan QB** (2018) Permian-Early Jurassic tectonic evolution of Kaiyuan-Yanji area in the eastern segment of the northern margin of the North China Block: [Dissertation]. Jilin University, Changchun. 1–120 (in Chinese).

**Guivel C, Lagabrielle Y, Bourgois J, Maury R, Fourcade S, Martin H and Arnaud N** (1999) New geochemical constraints for the origin of ridge-subduction-related plutonic and volcanic suites from the Chile triple Junction (Taitao Peninsula and Site 862, LEG ODP141 on the Taitao Ridge). *Tectonophysics* **311**, 83–111.

**Hernández-Uribe D, Hernández-Montenegro JD, Cone KA and Palin RM** (2020) Oceanic slab-top melting during subduction: Implications for trace-element recycling and adakite petrogenesis. *Geology* **48**, 216–220.

**Hoskin PWO** (2005) Trace–element composition of hydrothermal zircon and the alteration of Hadean zircon from the Jacks Hills, Australia. *Geochimica Acta* **69**, 637–648.

**Hu ZC, Liu YS, Gao S, Liu WG, Zhang W, Tong XR, Lin L, Zong KQ, Li M, Chen HH, Zhou L and Yang L** (2012) Improved in situ Hf isotope ratio analysis of zircon using newly designed Xskimmer cone and jet sample cone in combination with the addition of nitrogenby laser ablation multiple collector ICP-MS. *Journal of Analytical Atomic Spectrometry* **27**, 1391–1399.

**Huang BC, Yan YG, Piper JDA, Zhang DH, Yi ZY, You S, Zhou TH** (2018) Paleomagnetic constraints on the paleogeography of the East Asian blocks during late Paleozoic and early Mesozoic times. *Earth-Science Review* **186**, 8–36.

**Irvine TH and Baragar WRA** (1971) A guide to the chemical classification of the common volcanic rocks. *Canadian Journal of Earth Sciences* **8**, 523–548.

**Jia DC, Hu RZ, Lu Y and Qiu XL** (2004) Collision belt between the Khanka block and the North China block in the Yanbian Region, Northeast China. *Journal of Asian Earth Sciences* **23**, 211–219.

**Jian P, Liu DY, Kröner A, Windley BF, Shi YR, Zhang W, Zhang FQ, Miao LC, Zhang LQ and Tomurhuu D** (2010) Evolution of a Permian intraoceanic arc–trench system in the Solonker suture zone, Central Asian Orogenic Belt, China and Mongolia. *Lithos* **118**, 169–190.

**Jing Y, Ge WC, Dong Y, Yang H, Ji Z, Bi HY, Zhou HY and Xing DH** (2020) Early–Middle Permian southward subduction of the eastern Paleo–Asian Ocean: Constraints from geochronology and geochemistry of intermediate–acidic volcanic rocks in the northern margin of the North China Craton. *Lithos* **364–365**, 105491.

**Jing Y, Ge WC, Dong Y, Yang H, Ji Z, Bi HY, Zhou HY and Xing DH** (2021) Middle–late permian I-type granitoids from the Diaobingshan region in the northern margin of the North China Craton: insight into southward subduction of the Paleo–Asian Ocean. *International Geology Review* **63**, 357–379.

**Jing Y, Ge WC, Dong Y, Yang H, Ji Z, Bi JH, Zhou HY and Xing DH** (2022b) Final-stage Southward Subduction of the Eastern Paleo-Asian Ocean: Evidence from the Middle Permian Mafic Intrusions in the Northern Margin of the North China Craton. *Acta Geologica Sinica* (English Edition) **96**, 81–99.

**Jing Y, Ge WC, Santosh M, Dong Y, Yang H, Ji Z, Bi JH, Zhou HY and Xing DH** (2022a) Generation of Nb–enriched mafic rocks and associated Jingadakitic rocks from the southeastern Central Asian Orogenic Belt: Evidence of crust–mantle interaction. *Geoscience Frontiers* **13**,101341.

**Kay RW and Kay SM** (1993) Delamination and delamination magmatism. *Tectonophysics* **219**, 177–189.

**Kay RW and Kay SM** (2002) Andean adakites: three ways to make them. *Acta Petrologica Sinica* **18**, 303–311.

**Kelemen PB** (1995) Genesis of high Mg andesites and the continental crust. *Contributions to Mineralogy and Petrology* **120**, 1–19.

**Koschek G** (1993) Origin and significance of the SEM cathodoluminescence from zircon. *Journal of Microscopy* **171**, 223–232.

**Li CD, Zhang FQ, Miao LC, Xie HQ, Xu YW** (2007) Zircon SHRIMP geochronology and geochemistry of Late Permian high–Mg andesites in Seluohe area, Jilin Province, China. *Acta Petrologica Sinica* **23**, 767–776.

**Li HD, Zhou JB and Wilde SA** (2022b) Nature and development of the South Tianshan–Solonker suture zone. *Earth–Science Reviews* **233**, 104189.

**Li S, Chung SL, Wilde SA, Jahn BM, Xiao WJ, Wang T and Guo QQ** (2017) Early-Middle Triassic high Sr/Y granitoids in the southern Central Asian Orogenic Belt: Implications for ocean closure in accretionary orogens. *Journal of Geophysical Reserch: Solid Earth* **122**, 2291–2309.

**Li S, Wilde SA, Wang T, Xiao WJ and Guo QQ** (2016) Latest Early Permian granitic magmatism in southern Inner Mongolia, China: Implications for the tectonic evolution of the southeastern Central Asian Orogenic Belt. *Gondwana Research* **29**, 168–180.

**Liu J, Zhang J, Liu ZH, Yin CQ, Zhao C, Yu XY, Chen Y, Tian Y and Dong Y** (2020) Petrogenesis of Permo–Triassic intrusive rocks in Northern Liaoning Province, NE China: Implications for the closure of the eastern Paleo–Asian Ocean. *International Geology Review* **62**, 754–780.

**Liu YJ, Feng ZQ, Jiang LW, Jin W, Li WM, Guan QB, Wen QB and Liang CY** (2019) Ophiolite in the eastern Central Asian Orogenic Belt, NE China. *Acta Petrologica Sinica* **35**, 3017–3047 (in Chinese with English Abstract).

**Liu YJ, Li WM, Feng ZQ, Wen QB, Neubauer F and Liang CY** (2017) A review of the Paleozoic tectonics in the eastern part of Central Asian Orogenic Belt. *Gondwana Research* **43**, 123–148.

**Liu YJ, Li WM, Ma YF, Feng ZQ, Guan QB, Li SZ, Chen ZX, Liang CY and Wen QB** (2021) An orocline in the eastern Central Asian Orogenic Belt. *Earth–Science Reviews* **221**, 103808.

**Liu YJ, Ma YF, Feng ZQ, Li WM, Li SZ, Guan QB, Chen ZX, Zhou T and Fang QA** (2022) Paleozoic Orocline in the eastern Central Asian Orogenic Belt. *Acta Geologica Sinica* **96**, 3468–3493(in Chinese with English Abstract).

**Liu YJ, Xiao WJ, Ma YF, Li SZ, Peskov AY, Chen ZX, Zhou T and Guan QB** (2023) Oroclines in the Central Asian Orogenic Belt. *National Science Review* **10**, 17–19.

**Liu YS, Wang XH, Wang DB, He DT, Zong KQ, Gao CCG, Hu ZC and Gong HJ** (2012) Triassic high-Mg adakitic andesites from Linxi, Inner Mongolia: Insights into the fate of the Paleo-Asian ocean crust and fossil slab-derived melt-peridotite interaction. *Chemical Geology* **328**, 89–108.

**Ludwig KR** (2003) *User's Manual for Isoplot 3.0: A Geochronological Toolkit for Microsoft Excel*. vol. **4**. Berkeley Geochronology Center, p. 1–71 (special publication).

**Macpherson CG, Dreher ST, Thirwall MF** (2006) Adakites without slab melting: high pressure differentiation of island arc magma, Mindanao, the Philippines. *Earth and Planetary Science Letters* **243**, 581–593.

**Maniar PD and Piccoli PM** (1989) Tectonic discrimination of granitoids. *GSA Bulletin* **101**, 635–643.

**Peccerillo A and Taylor SR** (1976) Geochemistry of Eocene calc–alkaline volcanic rocks from the Kastamonu area, northern Turkey. *Contributions to Mineralogy and Petrology* **58**, 63–81.

**Rapp RP, Shimizu N, Norman MD and Applegate GS** (1999) Reaction between slab–derived melts and peridotite in the mantle wedge: experimental constraints at 3.8 GPa. *Chemical Geology* **160**, 335–356.

**Rapp RP and Watson EB** (1995) Dehydration melting of metabasalt at 8-32 kbar: Implications for continental growth and crust-mantle recycling. *Journal of Petrology* **36**, 891–931.

**Rudnick RL and Gao S** (2003) Composition of the continental crust. In *Treatise on geochemistry* (eds HD Holland, KK Turekian, RL Rudnick), p. 1–64. The Crust, vol. 3. Elseviere Pergamon: Oxford.

**Sajona FG, Maury RC, Bellon H, Cotton J, Defant MJ, Pubellier M and Rangin C** (1993) Initiation of subduction and the generation of slab melts in western and eastern Mindanao, Philippines. *Geology* **21**, 1007–1010.

**Sen C and Dunn T** (1994) Dehydration melting of a basaltic composition amphibolite at 1.5GPa and 2.0GPa: Implications for the origin of adakites. *Contributions to Mineralogy and Petrology* **117**, 394–409.

**Şengör AMC, Natal'in BA, Burtman VS** (1993) Evolution of the Altaid tectonic collage and Palaeozoic crustal growth in Eurasia. *Nature* **364**, 299–307.

**Shao JA, Tian W and Zhang JH** (2015) Early Permian cumulates in northern margin of North China Craton and their tectonic significances. *Earth Science* (China University) **09**, 1441–1457 (in Chinese with English abstract).

**Shen YJ, Chen B, Li JY, Sun JL, Zhao CJ, Zheng T and Liu JL** (2020) Geochemical characteristics, petrogenesis and geological significance of early Triassic high magnesium diorite in central Jilin province. *Journal of Heilongjiang University of Science and Technology* **30**, 481–489 (in Chinese with English abstract).

**Shi Y, Chen JS, Wei MH, Shi SS, Zhang C, Zhang LD and Hao YJ** (2020) Evolution of eastern segement of the Paleo-Asian Ocean in the Late Paleozoic: Geochronology and geochemistry constraints of granites in Faku area, North Liaoning, NE China. *Acta Petrologica Sinica* **36**, 3287–3308 (in Chinese with English Abstract).

**Shi Y, Liu ZH, Liu YJ, Shi SS, Wei MH, Yang JJ and Gao T** (2019) Late Paleozoic–Early Mesozoic southward subduction–closure of the Paleo–Asian Ocean: Proof from geochemistry and geochronology of Early Permian–Late Triassic felsic intrusive rocks from North Liaoning, NE China. *Lithos* **346–347**, 105165.

**Shi Y, Shi SS, Liu ZH, Wang L, Liu J, Chen JS, Yang F, Zhang C, Li B and Zhang LD** (2022) Back–arc system formation and extinction in the southern Central Asian Orogenic Belt: New constraints from the Faku ophiolite in north Liaoning, NE China. *Gondwana Research* **103**, 64–83.

**Song ZG, Han ZZ, Gao LH, Geng HY, Li XP, Meng FX, Han M, Zhong WJ, Li JJ, Du QX, Yan JL and Liu H** (2018) Permo–Triassic evolution of the southern margin of the Central Asian Orogenic Belt revisited: insights from Late Permian igneous suite in the Daheishan Horst, NE China. *Gondwana Research* **56**, 23–50.

**Soret M, Bonnet G, Agard P, Larson KP, Cottle JM, Dubacq B, Kylander–Clark ARC, Button M and Rividi N** (2022) Timescales of subduction initiation and evolution of subduction thermal regimes. *Earth Planetary Science Letters* **584**, 117521.

**Streckeisen A** (1976) To each plutonic rock its proper name. *Earth–Science Review* **12**, 1–33.

**Sun SS and McDonough WF** (1989) Chemical and isotopic systematics of oceanic basalts: Implications for mantle composition and processes. In *Magmatism in the Ocean Basins* (eds AD Saunders and MJ Norry), pp. 313–345. Geological Society, London, Special Publications no.42.

**Wang Q, Xu JF, Jian P, Bao ZW, Zhao ZH, Li CF, Xiong XL and Ma JL** (2006) Petrogenesis of adakitic porphyries in an extensional tectonic setting, Dexing, South China: Implications for the genesis of porphyry copper mineralization. *Journal of Petrology* **47**, 119–144.

**Wang Q, Zhao ZH, Bai ZH, Xiong XL, Mei HJ, Xu JF, Bao ZW and Wang YX** (2003) Carboniferous adakite and Nb-rich island arc basalt in Alatau Mountains, Xinjiang: Interaction between slab melt and mantle peridotite and crustal accretion. *Journal of Chinese Science Bulletin* **48**, 1342–1349 (in Chinese).

**Whalen JB, Currie KL, Chappell BW** (1987) A-type granites: Geochemical characteristics, discrimination and petrogenesis. *Contributions to Mineralogy and Petrology* **95**, 407–419.

**Wilde SA, Zhang XZ and Wu FY** (2000) Extension of a newly identified 500 Ma metamorphic terrane in North East China: Further U–Pb SHRIMP dating of the Mashan Complex, Heilongjiang Province, China. *Tectonophysics* **328**, 115–130.

**Windley BF, Alexeiev D, Xiao WJ, Kröner A and Badarch G** (2007) Tectonic models for accretion of the Central Asian Orogenic Belt. *Journal of the Geological Society of London* **164**, 31–47.

**Wood BJ and Turner SP** (2009) Origin of primitive high-Mg andesite: Constraints from natural examples and experiments. *Earth and Planetary Science Letters* **283**, 59–66.

**Wu FY, Jahn BM, Wilde S and Sun DY** (2000) Phanerozoic crustal growth: U–Pb and Sr–Nd isotopic evidence from the granites in northeastern China. *Tectonophysics* **328**, 89–113.

**Wu FY, Li XH, Zheng YF and Gao S** (2007b) Lu-Hf isotopic systematics and their applications in petrology. *Acta Petrologica Sinica* **23**, 185–220 (in Chinese with English Abstract).

**Wu FY, Sun DY, Ge WC, Zhang YB, Grant ML, Wilde SA and Jahn BM** (2011) Geochronology of the Phanerozoic granitoids in northeastern China. *Journal of Asian Earth Sciences* **41**, 1–30.

**Wu FY, Yang YH, Xie LW, Yang JH and Xu P** (2006) Hf isotopic compositions of the standard zircons in U-Pb geochronology. *Chemical Geology* **234**, 105–126.

**Wu FY, Zhao GC, Sun DY, Wilde SA and Yang JH** (2007a) The Hulan Group: Its role in the evolution of the Central Asian orogenic belt of NE China. *Journal of Asian Earth Sciences* **30**, 542–556.

**Xiao WJ, Windley BF, Hao J and Zhai MG** (2003) Accretion leading to collision and the Permian Solonker suture, Inner Mongolia, China: Termination of the Central Asian orogenic belt. *Tectonics* **22**, 1069.

**Xiao WJ, Windley BF, Sun S, Li JL, Huang BC, Han CM, Yuan C, Sun M and Chen HL** (2015) A tale of amalgamation of three Permo–Triassic collage systems in Central Asia: Oroclines, sutures, and terminal accretion. *Annual Review of Earth and Planetary Sciences* **43**, 477–507.

**Xu B, Charvet J, Chen Y, Zhao P, Shi GZ** (2013) Middle Paleozoic convergent orogenic belts in western Inner Mongolia (China): framework, kinematics, geochronology and implications for tectonic evolution of the Central Asian Orogenic Belt. *Gondwana Research* **23**, 1342–1364.

**Xu JF, Shinjo R, Defant MJ, Wang Q and Rapp RP** (2002) Origin of Mesozoic adakitic intrusive rocks in the Ningzhen area of east China: Partial melting of delaminated lower continental crust? *Geology* **30**, 1111–1114.

**Xu WL, Gao S, Wang QH, Wang DY and Liu YS** (2006) Mesozoic crustal thickening of the eastern North China craton: Evidence from eclogite xenoliths and petrologic implications. *Geology* **34** 721–724.

**Xue JX** (2021) Characteristics of Early Permian-Middle Triassic Volcanic Rocks in Faku-Kaiyuan, Eastern Part of the Northern Margin of the North China Block and Their Tectonic Significance: [Dissertation]. Jilin University, Changchun. 1–77 (in Chinese).

**Yang JH, Wu FY, Shao JA, Wilde SA, Xie LW and Liu XM** (2006) Constraints on the timing of uplift of the Yanshan Fold and Thrust Belt, North China. *Earth and Planetary Science Letters* **246**, 336–352.

**Yin JY, Yuan C, Sun M, Long XP, Zhao GC, Wong KP, Ge HY and Cai KD** (2010) Late Carboniferous High-Mg dioritic dikes in Western Junggar, NW China: Geochemical features, petrogenesis and tectonic implications. *Gondwana Research* **17**, 145–152.

**Yogodzinski GM, Kay RW, Volynets ON, Koloskov AV and Kay SM** (1995) Magnesian andesite in the western Aleutian Komandorsky region: implications for slab melting and processes in the mantle wedge. *Geological Society of America Bulletin* **107**, 505–519.

**Yuan LL, Zhang XH, Xue FH, Lu YH and Zong KQ** (2016) Late Permian high–Mg andesite and basalt association from northern Liaoning, North China: Insights into the final closure of the Paleo–Asian ocean and the orogen–craton boundary. *Lithos* **258–259**, 58–76.

**Zhang CY, Zhang XZ and Qiu DM** (2007) Ziron U-Pb isotope age and implation of plagioam phibolite in Qing long cun Group, Yanbian area. *Journal of Jilin University* (Earth Science Edition) **37**, 672–677 (in Chinese with English abstract).

**Zhang L** (2021) Late Paleozoic tectonic evolution of the eastern segment of the northern margin of the North China Craton—Study on tectonic attributes of the Xia'ertai Group, Northern Liaoning Province (China): [Dissertation]. Jilin University, Changchun. 1–90 (in Chinese).

**Zhang N, Wang CB, Liu ZH, Xu ZY, Li G, Xuan YF, Gao Y and Wang C** (2022) Tectonic evolution of the Late Paleozoic-Early Mesozoic orogenic belt in the eastern segment of the northern margin of the North China Block: Evidence from meta-volcanic rocks of Jianshanzi, Northern Liaoning Province. *Acta Petrologica Sinica* **38**, 2323–2344 (in Chinese with English Abstract).

**Zhang Q, Qian Q, Wang EQ, Wang Y, Zhao TP, Hao J and Guo GJ** (2001) An east China plateau in Mid-Late yanshanian period: implication from adakites. *Chinese Journal of Geology* (Scientia Geologica Sinica), 248–255+8(in Chinese with English Abstract).

**Zhang XH, Su WJ and Wang H** (2005) Zircon SHRIMP geochronology of the Faku tectonites in the northern Liaoning Province: Implications for the northern boundary of the North China Craton. *Acta Petrologica Sinica* **21**, 135–142 (in Chinese with English Abstract).

**Zhang XH, Zhang HF, Wilde SA, Yang YH and Chen HH** (2010) Late Permian to Early Triassic mafic to felsic intrusive rocks from North Liaoning, North China: Petrogenesis and implications for Phanerozoic continental crustal growth. *Lithos* **117**, 283–306.

**Zhao P, Xu B, Tong Q, Chen Y, Faure M** (2016) Sedimentological and geochronological constraints on the Carboniferous evolution of central Inner Mongolia, southeastern central Asian Orogenic Belt: Inland sea deposition in a post-orogenic setting. *Gondwana Research* **31**, 253–270.

**Zhao QY, Li CF, Li DC, Chen YJ** (2008) Dating for zircons from gabbro dike of Wudaogou Group in Yanbian area and its geological significance. *Global Geology* **27**, 150–155 (in Chinese with English abstract).

**Zhou ZB, Pei FP, Wang ZW, Cao HH, Lu SM, Xu WL and Zhou H** (2018) Geochronology and geological implications of Fangniugou volcanic rocks in Yitong area, central Jilin Province. *Global Geology* **37**, 46–55 (in Chinese with English Abstract).